Growth and characterization of novel thin films for microelectronic applications

by

Mahmoud Vahidi

A Dissertation Presented in Partial Fulfillment
of the Requirements for the Degree
Doctor of Philosophy

Approved July 2013 by the
Graduate Supervisory Committee:

Nathan Newman, Chair
Tingyong Chen
Rakesh Singh
Terry Alford

ARIZONA STATE UNIVERSITY

August 2013

ABSTRACT

I studied the properties of novel $Co_2FeAl_{0.5}Si_{0.5}$ (CFAS), $ZnGeAs_2$, and FeS_2 (pyrite) thin films for microelectronic applications ranging from spintronic to photovoltaic.

CFAS is a half metal with theoretical spin polarization of 100%. I investigated its potential as a spin injector, for spintronic applications, by studying the critical steps involved in the injection of spin polarized electron populations from tunnel junctions containing CFAS electrodes. Epitaxial CFAS thin films with $L2_1$ structure and saturation magnetizations of over 1200 emu/cm^3 were produced by optimization of the sputtering growth conditions. Point contact Andreev reflection measurements show that the spin polarization at the CFAS electrode surface exceeds 70%. Analyses of the electrical properties of tunnel junctions with a superconducting Pb counter-electrode indicate that transport through native Al oxide barriers is mostly from direct tunneling, while that through the native CFAS oxide barriers is not.

$ZnGeAs_2$ is a semiconductor comprised of only inexpensive and earth-abundant elements. The electronic structure and defect properties are similar in many ways to GaAs. Thus, in theory, efficient solar cells could be made with $ZnGeAs_2$ if similar quality material to that of GaAs could be produced. To understand the thermochemistry and determine the rate limiting steps of $ZnGeAs_2$ thin-film synthesis, the (a) thermal decomposition rate and (b) elemental composition and deposition rate of films were measured. It is concluded that the $ZnGeAs_2$ thin film synthesis is a metastable process with an activation energy of 1.08±0.05 eV for the kinetically-limited decomposition rate and an evaporation coefficient of ~10^{-3}. The thermochemical analysis presented here can

be used to predict optimal conditions of $ZnGeAs_2$ physical vapor deposition and thermal processing.

Pyrite (FeS_2) is another semiconductor that has tremendous potential for use in photovoltaic applications if high quality materials could be made. Here, I present the layer-by-layer growth of single-phase pyrite thin-films on heated substrates using sequential evaporation of Fe under high-vacuum followed by sulfidation at S pressures between 1 mTorr and 1 Torr. High-resolution transmission electron microscopy reveals high-quality, defect-free pyrite grains were produces by this method. It is demonstrated that epitaxial pyrite layer was produced on natural pyrite substrates with this method.

DEDICATION

This work is dedicated to my beloved parents who have made me stronger, better, and more fulfilled than I could ever have imagined.

ACKNOWLEDGMENTS

First and foremost, I am highly grateful to my advisor Prof. Nathan Newman for his constant advice, great enthusiasm, and consistent encouragement. I especially appreciate how he has guided me through this challenging experimental work and in the preparation of this dissertation. His unique way of approaching problems and the profound knowledge he has contributed will always be remembered.

I am particularly grateful to Dr. Rakesh Singh for his useful help, and for accepting to serve on my dissertation committee. I am also very grateful to Dr. Chen for his acceptance to serve on my dissertation committee and useful help for PCAR measurement. I'm very thankful to Prof. Alford for his willingness to serve on my dissertation committee.

I am especially thankful to Dr. Stephen Lehner for all his continuous support and valuable help during experimentation, characterization, and subsequent data analysis of pyrite project. I am very thankful to our collaborators Dr. Srini Krishnamurthy and Dr. Zhi Yu at SRI, Menlo Park, California, USA for their contribution in CFAS project. I am thankful to Mr. Shengke Zhang, Mr. Cameron Kopas, and Mr. You Li from Newman Research group for their help on experimentation and characterization of the samples. I'm also grateful to Dr. Lei Yu for his useful help during data analysis of my projects.

I wish to thank Mr. James Maker in ASU machine shop for his useful help on fabricating the devices. I am also very thankful to Mr. Richard Hanley in Newman group for all his support on fixing and making the equipment running in a good shape.

I wish to extend my gratitude to Dr. Amaneh Tasooji for her help and friendly advice when I came to ASU. I also wish to thank my friend Ronak for all her help and support.

I am obliged to colleagues within Newman research group, Mr. Mengchu Hunag, Mr. Makram Abd El Qader, Mr. Kevin Bunish and Mr. Lingtau Leo for their support and friendship.

Finally, I am also very thankful to all the other faculty and staff in the department of Materials Science at Arizona State University who have been really helpful in different capacities throughout my graduate education.

This project was supported by NSF grant number 0964955. The use of facilities in the LeRoy Eyring Center for Solid State Science at Arizona State University is acknowledged.

TABLE OF CONTENTS

Page

LIST OF TABLES

Table Page

LIST OF FIGURES

Figure Page

Chapter 1

INTRODUCTION

At the Fermi level, half metal ferromagnets (HFMs) have a metallic band structure in one spin channel and a semiconductor energy gap in the other [1, 2]. Thus, HFMs have 100% spin polarization at the Fermi level [3]. Since the electrode's spin polarization can limit the spin injection efficiency of spintronic devices, HFMs proposed as ideal candidates for these applications [4, 5]. However, the injection efficiency of most HFMs measured to date is far below 100% and is strongly temperature dependent [4]. This presumably arises from the presence of spin-wave excitations and the narrow energy separation between the Fermi level and one, or both, of the minority channel band edges [4].

In the next chapter, I reported the results of study to explore spin injection from the Heusler alloy $Co_2FeAl_{0.5}Si_{0.5}$ (CFAS). Since the Fermi energy of the majority spin channel in CFAS is predicted to lie in the middle of the large minority band gap [6], both the polarization at the surface and the injection efficiency at room temperature are expected to be very high. In my effort to understand and enhance spin injection, I have systematically (a) optimized the magnetic properties of CFAS thin films, (b) evaluated the spin polarization at the surface using the point contact Andreev reflection (PCAR) method and (c) determined the fraction of direct tunneling from tunneling spectroscopy measurements using a superconducting Pb counter-electrode.

Major obstacles for using solar energy as a primary source of electricity are the production costs, toxicity, and availability of rare elements for current photovoltaic devices made of crystalline Si, CIGS [$(CuIn)_xGa_{1-x}Se_2$], and CdTe [7]. Therefore, the use of earth abundant elements is essential to meet a terawatt-scale production target for an affordable electricity supply using photovoltaic devices [8].

II-IV-V compounds have attractive material properties including appropriate band gaps for photovoltaic, high photon absorption, and defect robustness [8]. $ZnGeAs_2$ films, from this group, possess hole mobility of greater than 50 $cm^2/V \cdot sec$ [9-11], minority carrier lifetimes of ~150 ns [12], band gap of 1.1 eV, and a lattice constant match to Ge and GaAs. These properties, in conjunction with the natural abundance of its constituents, suggest that this material is a good candidate to make low-cost, efficient photovoltaic cells [8]. In the third chapter, I presented the thermochemistry and growth optimization for $ZnGeAs_2$ semiconductor compound for photovoltaic applications.

Pyrite (FeS_2), a semiconductor composed of inexpensive, non-toxic elements, has a bandgap of ~0.95 eV [13] and an absorption coefficient (6.5×10^5 cm^{-1}) higher than conventional direct bandgap semiconductors, including GaAs [14]. These facts have inspired scientists to consider pyrite as a potential candidate for terawatt-scale photovoltaic systems [7, 13, 14]. However, there has been limited progress synthesizing thin films of sufficient quality to produce efficient solar cells, largely due to high S pressure needed during synthesis. In the fourth chapter, I described a layer-by-layer growth technique that produces high-quality, high-purity and epitaxial pyrite thin films

using sequential evaporation of Fe under high vacuum followed by sulfidation at pressures ≥1 mTorr and compare the results with those using traditional MBE growth.

Chapter 2

SYNTHESIS AND CHARACTERIZATION OF CO2FEAL0.5SI0.5, A NOVEL HALF METAL THIN FILM FOR SPINTRONIC APPLICATIONS

2.1. Introduction

Half metal ferromagnets (HFMs) are materials which can be considered hybrids between metals and semiconductors. At the Fermi level, they have metallic band structure in one spin direction and a semiconductor energy gap in another direction [1, 2]. Electron spin polarization (P) is defined as the ratio of the density of up-spin and down-spin states at the Fermi level (E_f), eq. 1 [15]. Thus, HFMs have 100% spin polarization at the Fermi level (E_F) [4].

$$P=(D\uparrow(E_F)-D\downarrow(E_F))/(D\uparrow(E_F)+D\downarrow(E_F)) \quad \text{eq. 1}$$

The efficiency of spin-dependent devices, such as magnetic sensors and magnetic random access memories, will be maximized if the current is 100% spin polarized [4, 5]. Therefore, HFMs have been proposed as ideal candidates for spintronics [4]. However, all the so far reported HFMs show strong temperature dependence of their spin polarizations, which limits their practical applications [4]. The temperature dependence is mainly due to spin-wave excitation and narrow energy separation between the majority channel Fermi level and the minority channel conduction or valence band edge [4].

Recently, Co-based full-Heusler alloys Co_2YZ (Y: transition metal, Z: main group element) have been given considerable attention, since they are predicted to be HFMs

even at room temperature as a result of their high magnetization and high Curie temperature [5, 6]. A promising candidate from this family is $Co_2FeAl_{0.5}Si_{0.5}$ (CFAS), since it is theoretically estimated that the majority channel E_F for CFAS lies in the middle of the large minority channel band gap, minimizing the temperature dependence of spin polarization [6].

Properties of the devices mentioned above are sensitive to the spin polarization of ferromagnetic electrodes, barrier materials, and structures of the interface between the barrier and electrodes [4-6]. Therefore, experimental measurements of spin polarization (P) and characterization of the barrier are important for understanding these materials.

Spin polarization can be measured by fabricating a magnetic tunneling junction (MTJ) which consists of two ferromagnetic layers separated by a tunnel barrier (insulator), schematically shown in Fig. 1-a. Then the tunneling magnetoresistance (TMR) effect can be adopted to evaluate spin polarization [4]. TMR can be determined by measuring R_{ap} and R_P, the tunnel resistance when the magnetizations of the two electrodes are aligned antiparallel and parallel respectively. The parallel configuration has lower resistance than the antiparallel configuration, Fig 1-b. Julliere's formula, eq. 2, can be used to estimate the spin polarization of the electrodes from TMR measurements. P_1 and P_2 are the electron spin polarization of the top and bottom electrodes [4-6].

$$TMR=(R_{ap}-R_p)/ R_p =P_1P_2/(1-P_1P_2) \qquad \text{eq. 2}$$

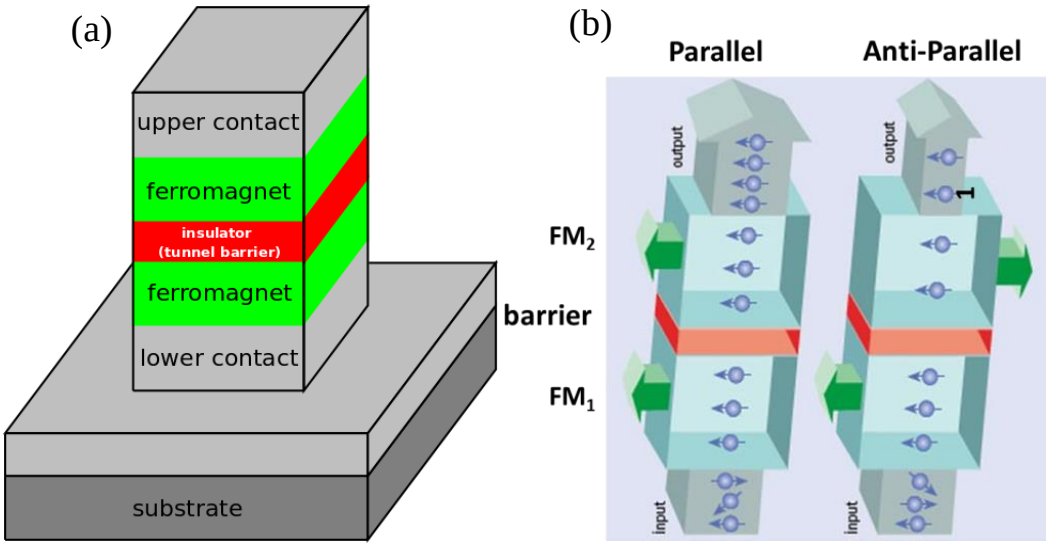

Fig. 1. Schematic of a) magnetic tunneling junction structure (MTJ) [16], b) current passing through MTJ when it has parallel and antiparallel configuration [17].

However, the P value inferred from the TMR measurements analyzed using the above formula can contain large errors due to the uncertainty in the assumed degree of spin polarization of the counter-electrode, and the influence introduced by an interfacial effect. Therefore, the P values may differ from the intrinsic spin polarization of the electrode materials [18]. In addition, TMR measurement is challenging to perform, since the sample must be incorporated into a high-quality pinhole-free tunnel junction [19]. Spin-polarized photoemission spectroscopy can also be used to directly measure the spin polarization, but is very sensitive to the surface quality and currently lacks the required energy resolution (1 meV) [19]. Another technique that can be used for spin polarization measurement is point contact Andreev reflection (PCAR) [19-21]. It is a simple method to measure P based on Andreev reflection phenomenon by touching a superconductor probe to the surface of sample, Fig. 2-a. Andreev reflection is a process that occurs at the interface between a metal and a superconductor without any oxide or tunnel-barrier layer in between. In this phenomenon, if the superconductor is in contact with a normal metal

having P=0 (equal density of spin down and up), an incident electron with an energy less than the superconducting energy gap at the interface forms a Cooper pair by reflecting a hole with opposite spin orientation at the interface. Once the Cooper pair forms it can pass into the semiconductor, which allows super-current to flow at low voltages (Fig 2-b). In contrast, if the superconductor contacts a ferromagnet with a P=1 (only one spin orientation available at the Fermi level), there is no available state for the opposite spin orientation in the ferromagnet and the hole (with opposite spin orientation respect to the incident electron) cannot be reflected. Therefore, the hole and the incident electron cannot combine to form a Cooper pair. Thus, no current will flow, and conductance drastically decreases at low voltages, Fig. 2-c. The advantage of this method is that it does not require any tunnel barrier, special surface preparation, or special sample geometry [19]. However, it can only be used in the temperature range in which the probe is superconducting.

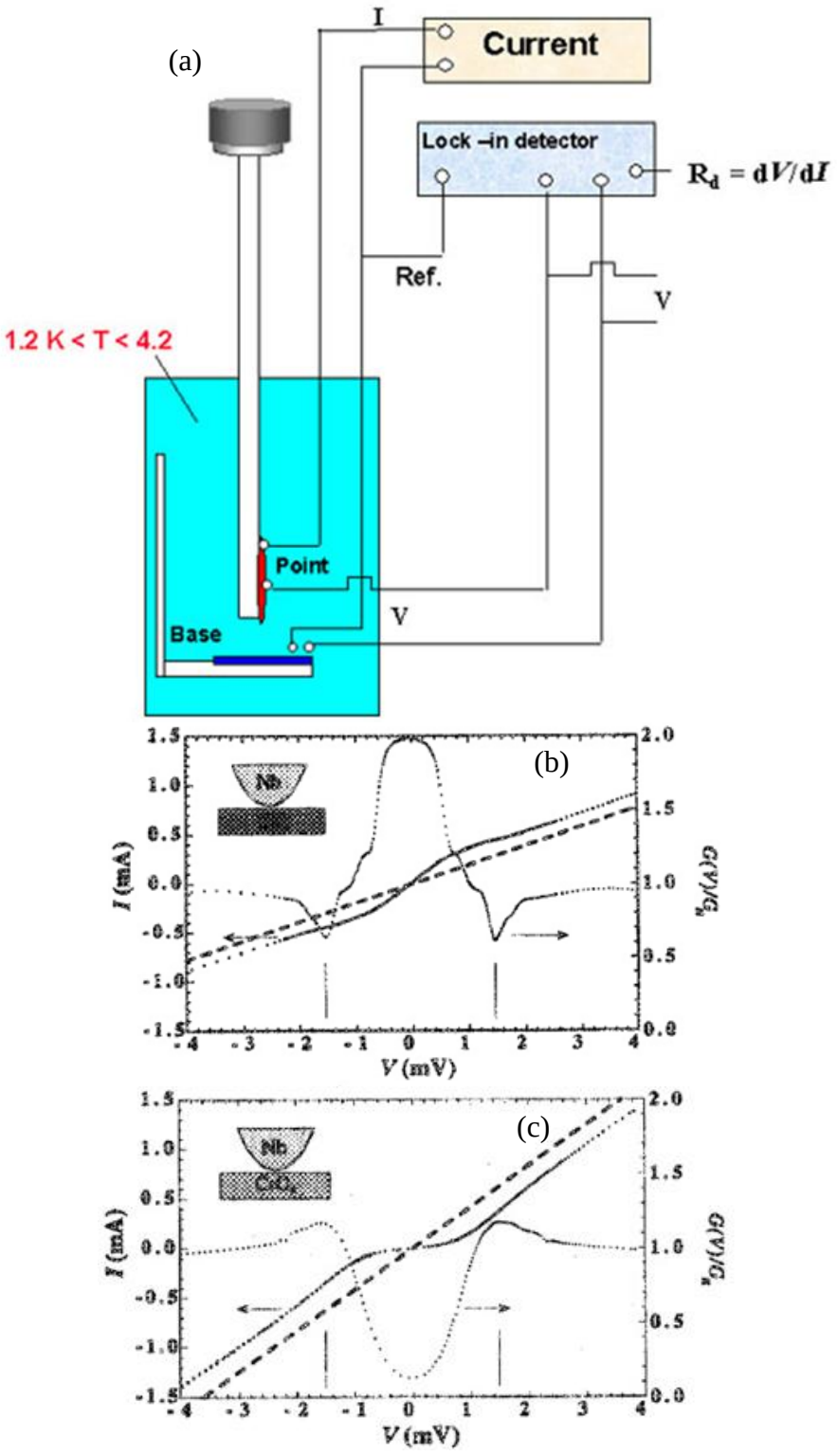

Fig. 2. a) Schematic of point contact Andreev reflection (PCAR) technique for spin polarization measurement, with an example of PCAR result for superconductor probe (Nb) touching the surface of b) Cu (P=0), c) CrO_2 (P=1) [19].

In this study, I investigated the effect of growth conditions on the structural and magnetic properties of CFAS thin films, and their spin polarization as measured by the PCAR method. In addition, the tunneling properties of native CFAS oxide and native Al oxide tunnel barriers deposited on the CFAS thin films were investigated.

2.2. Experimental procedure

CFAS films were prepared using magnetron sputtering in an ultra-high vacuum (UHV) chamber with a base pressure of 2×10^{-8} Torr. . Sputtering was performed using a stoichiometric CFAS (Co: 50%, Fe: 25%, Al: 12.5%, Si: 12.5%) target in 5 mTorr Argon gas at a plasma power of 100 W. MgO (100) and thermally oxidized silicon (SiO/Si (100)) were used as substrates. To compare and optimize the structural and magnetic properties of sputtered CFAS thin films, 1-step and 2-step processes were used. In the 1-step process, CFAS was deposited at an elevated growth temperature (Tg) without any further processing. In the 2-step process, the films deposited at room temperature were subjected to an in-situ annealing at higher temperatures (Ta).

Rutherford backscattered spectroscopy (RBS) measurements and analysis were used to infer the composition and thickness of the thin films. High resolution X-ray diffraction (PANalytical X'Pert PRO) was used for structural characterization. The magnetic properties of the films were characterized using a standard vibrating sample magnetometer (VSM) from 2 -1000 K (Quantum Design, Model PPMS with oven option). To analyze the surface quality and roughness of the thin films, an atomic force

microscopy (Veeco, Dimension 300) was used. Spin polarization of the CFAS films was measured by PCAR measurement and analysis at 4.2 K using a Pb probe.

To investigate an alternative growth method, CFAS thin films were grown by pulsed laser deposition (PLD) in a UHV chamber with a base pressure of 5×10^{-7} Torr. A 248 nm KrF excimer laser, pulsed at 10 Hz with an energy of 450 mJ/pulse, was used. A stoichiometric CFAS target was used. An Argon gas pressure was fixed at 5 mTorr during deposition.

A tunnel junction device, schematically represented in Fig. 3, was fabricated to study the tunneling properties of the barrier. The layer structure consists of a strip of CFAS, deposited on MgO, on the bottom, a tunnel barrier layer in the middle, and strips of the superconductor (Pb), perpendicular to CFAS strip, on top. The CFAS layer was deposited under the optimized growth conditions (highest spin polarization), obtained from the growth and characterization of CFAS thin film. The tunnel barrier layer was obtained both by naturally oxidizing the CFAS layer in air and synthesizing an Al oxide layer[1]. To synthesize the Al oxide layer, the surface of CFAS layer was first cleaned by ion milling. Next, a 40 Å Al layer was deposited by thermal evaporation in the same chamber at a base pressure of 1.8×10^{-8} Torr. Oxidization of the Al layer was performed in air for 4 hours. The CFAS strip was fabricated by photolithography and etching with a reactive ion etcher (RIE) using Ar gas. A layer of Ge was deposited to prevent any unwanted shorting between the CFAS layer and the Pb layer during measurement at low

[1] The presence of metallic Al after oxidation will not significantly affect the tunneling measurements with the superconducting Pb electrodes. However, the Al thickness should be reduced to eliminate unwanted spin-flip scattering in the excess Al for spintronic devices

temperature. Finally, the Pb layer was fabricated on top using a shadow mask and thermal evaporation. The fabricated device was dipped in the liquid helium dewar and the electrical characteristics of the device were measured using a 4 point measurement in the geometry presented in Fig. 3-b.

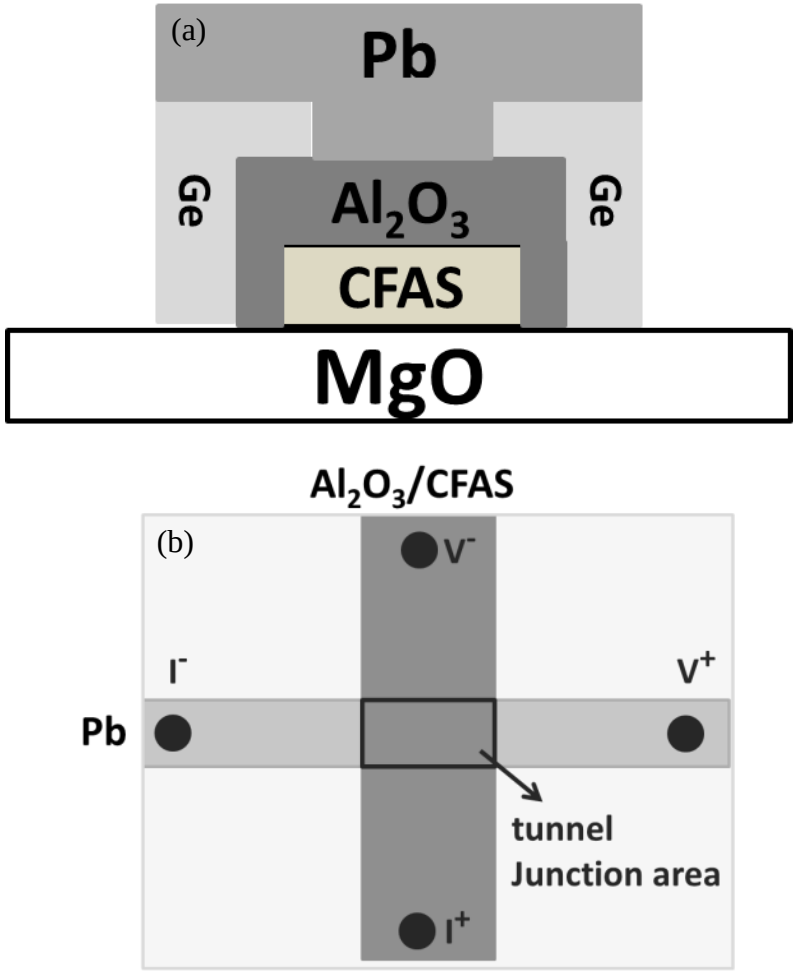

Fig. 3. Schematic of tunnel junction structure, a) side view, b) top view of the junction and the geometry of four point measurement.

2.3. Results and discussion

RBS results showed that the CFAS thin films grown by sputtering were stoiciometric with a thickness about 500 Å. Fig. 4 shows an example of the magnetic

hysteresis loops of CFAS sputtered thin films measured by VSM. As indicated in the plot, the magnetic properrties of the thin film, magnetization (M_s) and corsivity (H_c), can be derived form this plot.

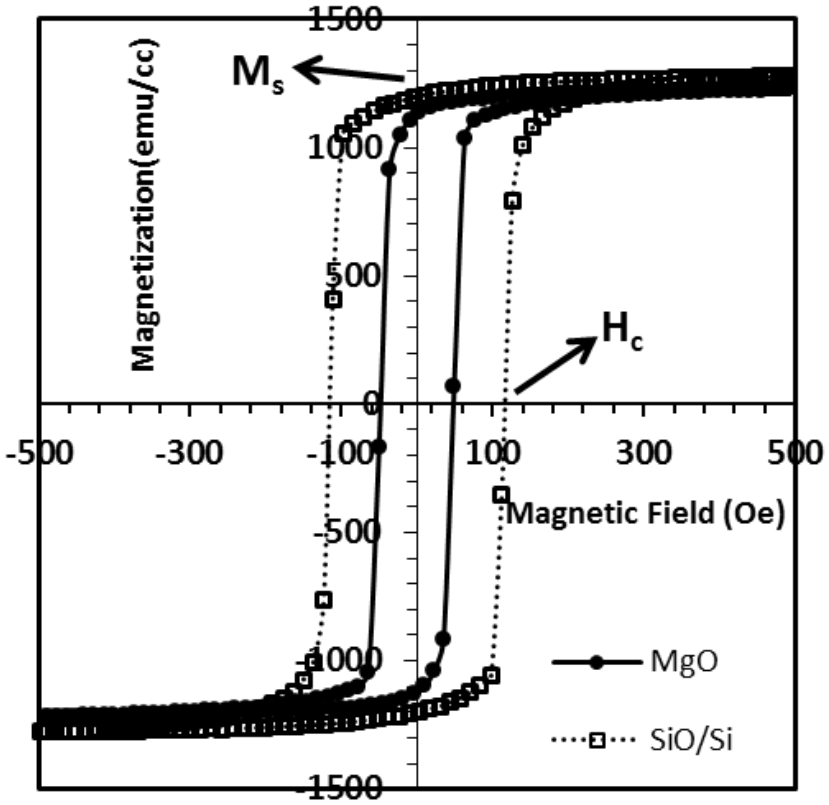

Fig. 4. Magnetic properties of CFAS films sputterd on MgO and SiO_x/Si at RT, and then anneald in-situ at 600 °C.

Fig. 5-a and b show the effect of annealing temeprature on the magnetic properties of thin films synthesized with the 2-step procedure on MgO and SiO_x/Si substrates, respectively. A high magnetization of ~1250 emu/cc was achieved with the 2-step procedure on MgO substrate by annealing at 600 °C. As can be seen, magnetization increases with annealing temperaure, in general, independent of substrates type. This increase can be releated to the increase in degree of ordering with increasing annealing

temperature (T_a) [6]. As T_a increases from room temperature to 500 °C, the corcevity of films drops gradually. However, as T_a is greater than 500 °C, coercivity starts increaing rapidly. The film sputtered on SiO_x/Si has a comparable M_s with the films sputtered on MgO, but, the coercivity is significantly higher, Fig 5-b. The same trend has been reported by Wong et al. for CFAS films grown on MgO and SiO_x/Si substrates with a 20-nm MgO buffer layer [5, 6]. Fig. 6, compares the magnetic propertied vs. temperature of the thin films that I sputtered on MgO with the results published by Wang et al. on CFAS sputtered on Si with a 30 nm MgO buffer layer [5]. As can be seen, comparable M_s and higher H_c to the reported values were obtained.

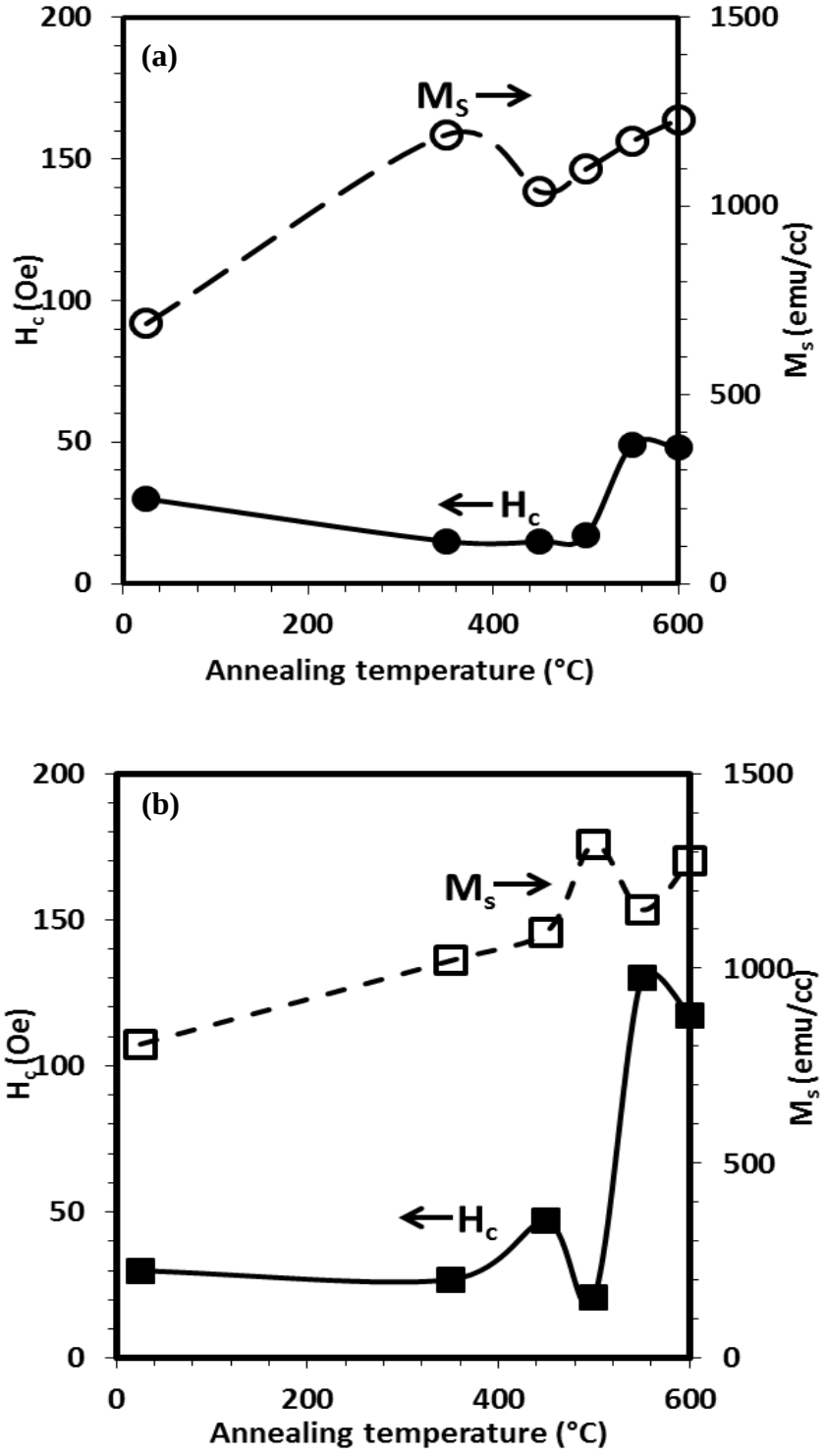

Fig. 5. Effect of annealing temperature on M_s and H_c of sputtered CFAS films on a) MgO and b) SiO_x/Si substrate.

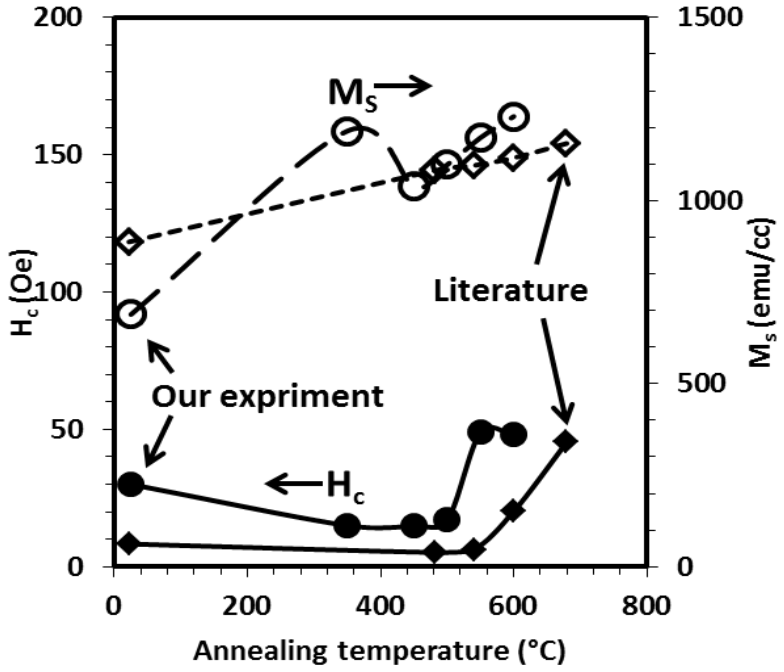

Fig. 6. Magnetic properties comparision between my exprimental results (circles) and the best reported results (diamonds) on CFAS thin films grown at RT and annealing in-situ at high temperature (2-step) [6].

To study the effect of susbtrate temperature on magnetic properties and crystal quality, CFAS thin films were sputtered at different substrate temperatures (1-step procedure). Fig. 7 shows the comparison between the magnetic properties of CFAS films prepared by the 1-step and 2-step processes. Films prepared by the 1-step procedure have comparable M_s to that of the 2-step procedure. However, the increase in H_c with increasing temperature is more sigificant for the 1-step procedure.

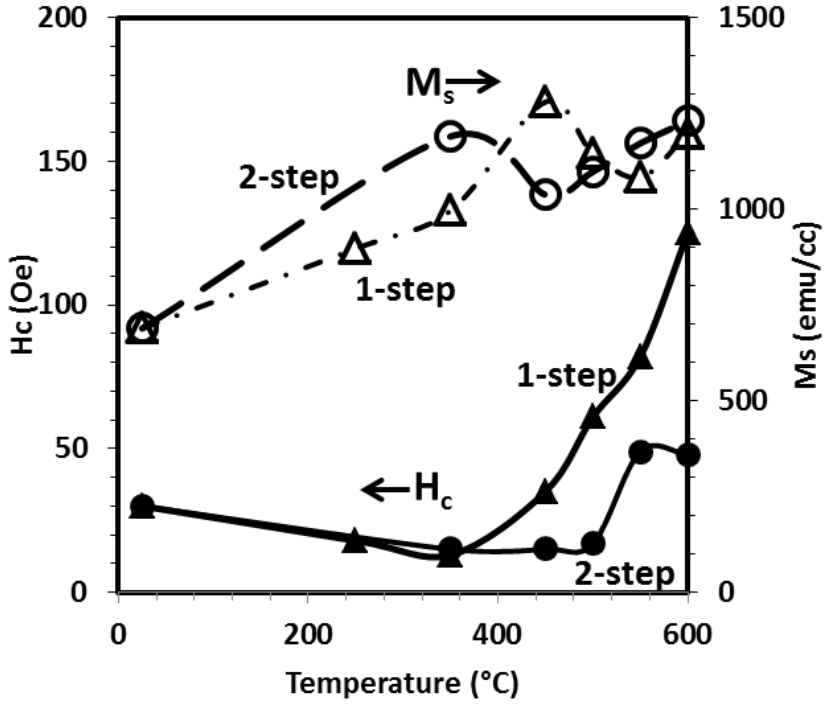

Fig. 7. Gorwth at high temprature (1-step, triangles) vs. growth at RT and annealing in-situ at high temperature (2-step, circles).

The magnetization vs. temperature characteristics was measured (Fig. 8) on a CFAS thin films, which exhibited excellent magnetic properties (i.e., inferred from hysteresis loop), prepared with the 2-step process at an annealing temperature of 600 °C. The magnetization of the CFAS thin films decreased by only 6% from 4.2 K to room temperature. The data were fit to the empirical equation, $M_s/M_{s0}=(1-(T/T_C)^{\alpha})^{\beta}$, to model both the low temperature regime ($T \rightarrow 0$), and high temperature regime ($T \rightarrow T_C$). In this equation, M_s is the magnetization, M_{s0} is zero-temperature magnetization, T_c is the Curie temperature, and α and β are fitting parameters. The magnetization value of 4.2 K were used for M_{s0}. The least squares fit to the data gives a Curie temperature of ~ 1150 ± 50 K, with the best fit to the experimental data when the fitting parameters α and β are set to

1.5 and 0.45, respectively. This results are in agreement with predicted high Curie temperature value of >1000 K for CFAS [22].The Curie temperatures for similar Co based Heusler alloys, Co_2MnSi [23] and Co_2FeSi [24], are 985 and 1100 K, respectively.

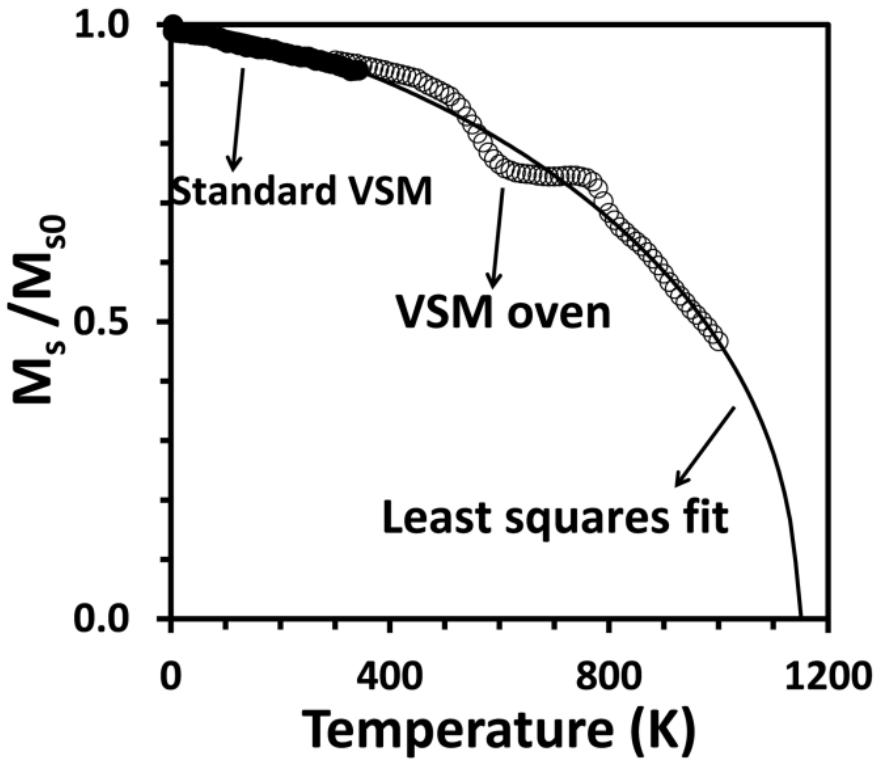

Fig. 8. Magnetization vs. temperature of the CFAS film sputterd on MgO at RT followed by annealing in-situ at 600 °C.

The surface quality of the CFAS thin films grown by sputtering was measured using AFM. The measurement, as shown in the Fig. 9, indicates that roughness of the films grown by 1-step process increases with temperature. The film grown at 600°C has largest surafce roughness (over 8 nm). In comparison, films grown in 2-step process are more smoother (Fig. 9).

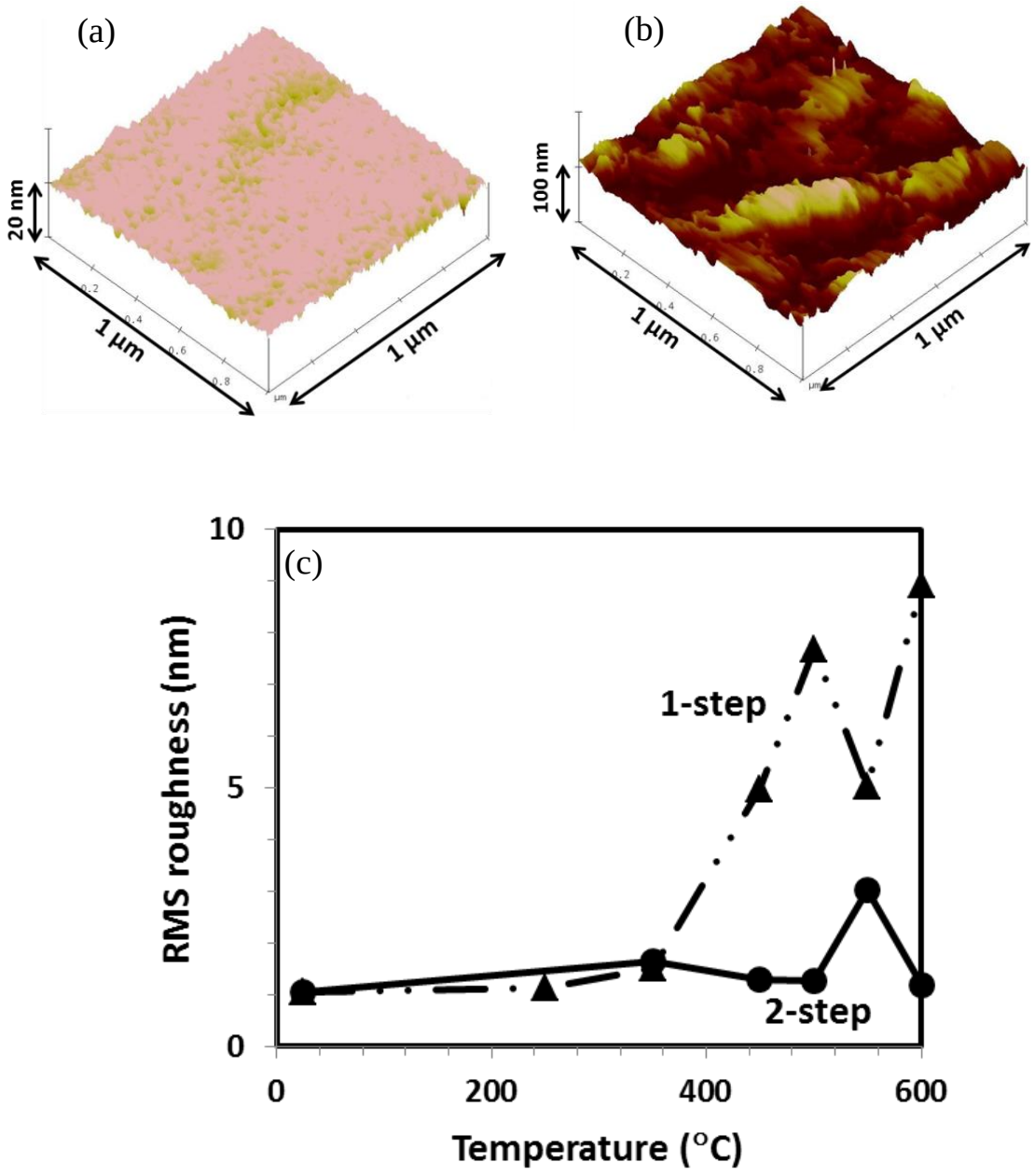

Fig. 9. AFM results of, a) sample grown at RT and annealed at 600 °C, b) sample grown at 600° C, and c) roughness of films grown with 1-step and 2-step process.

XRD was performed to characterize the crystal quality of the sputtered CFAS thin films, we. Fig. 10-a shows the XRD results from films grown with the 2-step process. No

CFAS peaks are detected by XRD, indicating that annealing at high temperature, up to 600 °C, did not result in crystalline film. This finding is in contrast to the results reported by Wang et al. [5] and Tezuka et al. [25] on CFAS thin films prepared by sputtering. They detected the (002) and (004) peaks of CFAS even in their as deposited film at RT. They reported as T_a increased, the intensity of the peaks increased as well. However, they deposited a buffer layer of MgO [5] and Cr [25] on their substrates prior to the CFAS deposition. This may be the reason they observed evidence of crystalline CFAS diffraction peaks in their XRD results.

However, epitaxial growth was detected on films sputtered at high substrate temperatures (1-step) using XRD. Fig. 10-b shows the presence of only (002) and (004) peaks in the XRD pattern for films sputtered on MgO without any buffer layer at T_g >250 °C, which indicates the formation of highly textured CFAS films. The intensity of the (002) and (004) CFAS peaks is enhanced with increasing growth temperature, indicating that crystal quality improves when exposed to larger thermal energies.

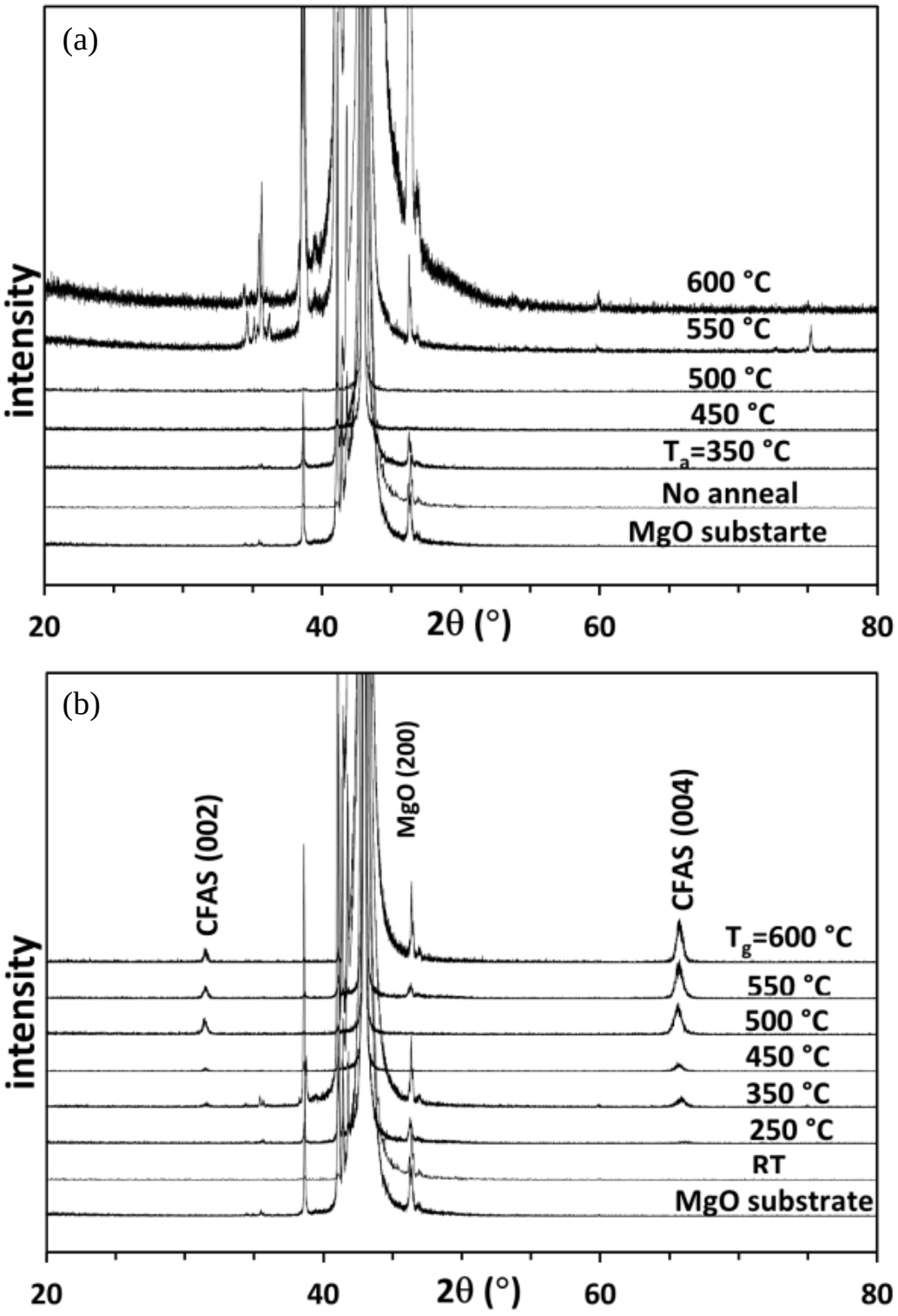

Fig. 10. Results of XRD, 2θ scan for films grown on MgO with a) 2-step, b) 1-step process.

Co_2YZ Heusler alloy has three ordering structures: A2, B2, and $L2_1$ [4-6]. Measurement of Φ scans from the off-axis Bragg peaks can be used to identify the ordering structure [5, 25]. The diffraction peak from the (111) or (311) superlattice corresponds to the $L2_1$ structure, and the peak from (222) superlattice reflection corresponds to the B2 structure. To confirm the nature and degree of ordering, the Φ scan measurements from the off-axis of the (111) peak was performed on the prepared CFAS films grown with the 1-step procedure. Fig. 11, shows the results of Φ scan for CFAS films sputtered at different T_g. Results show fourfold symmetry in the diffraction patterns, evidence of the $L2_1$ ordering structure, for CFAS films grown at growth temperatures over 350 °C. This is convincing proof that CFAS films were grown epitaxially and their structure is $L2_1$. In addition, the intensity of the (111) peak grows with increasing T_g, which indicates the degree of $L2_1$ ordering improves with increasing T_g. Tezuka et al. [25] and Wang et al. [5] reported detecting $L2_1$ by annealing sputtered samples at temperatures over 480 °C. Thus, it can be conclude that the CFAS films sputtered on MgO (001) substrates without any buffer layer at different T_g show epitaxy and the higher temperature growth improves the crystallization and ordering.

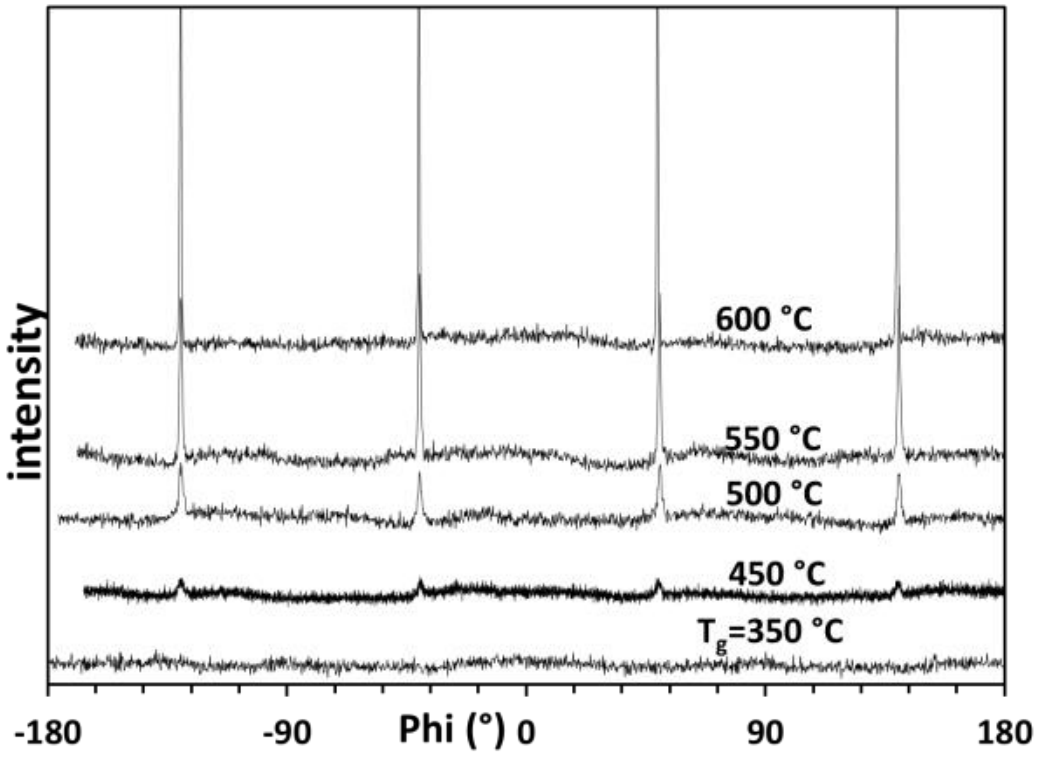

Fig. 11. Results of XRD, Φ scan of the (111) peak for films grown with 1-step process.

The spin polarization values of CFAS inferred from TMR measurements, a technique that can contain large errors due to the uncertainty in the assumed degree of spin polarization of the counter-electrode, vary from 71% [5] to 90% [4]. To obtain an accurate value of spin polarization at the surface, PCAR measurements were carried out [20, 21]. Fig. 12 shows an example of Andreev reflection measurement results of CFAS films. Complete results of PCAR measurement on CFAS sputtered samples are summarized in table. 1. They clearly show that annealing at higher temperature results in greater spin polarization. The highest spin polarization of 73% is detected. This value is also significantly greater than the 60% measured directly on bulk CFAS [26].

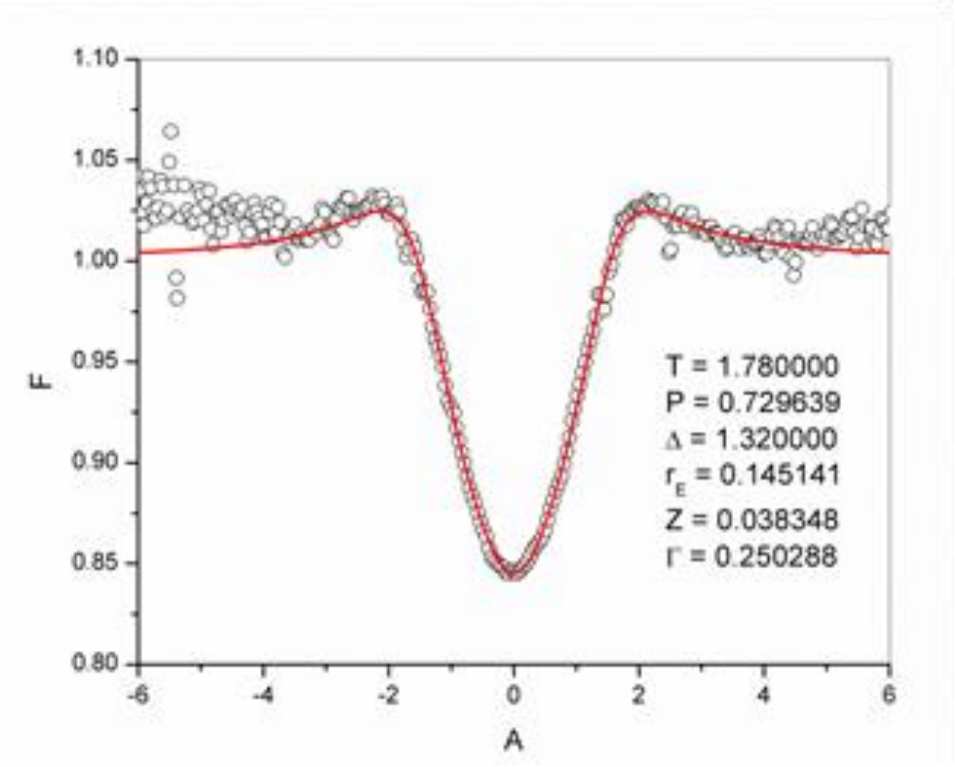

Fig. 12. Spin polarization measurement results of CFAS thin film sputtered at RT and in-situ annealed at 600° C.

Although the best films grown with the 1-step process have camparable magnetic properties and better crystal quality (i.e., $L2_1$ ordering), they are found to have smaller spin polarization at the surface (Table. 1) compared to the films prepared with the 2-step process with high annealing temperatures. This observation may be due to enhnaced surface roughness of films grown with the 1-step process. As illustrated in the AFM data shown in Fig. 10, films grown with 1-step at T_g>350 ° C are two to three times rougher than film grown with the 2-step procedure. The film grown at 600°C has largest surafce roughness (over 8 nm) and has only 50% surface spin polarization. In comparison, films grown in 2-step process are smoother (rms roughness ~1.3 nm) and have larger surafce spin polarization (Table. 1).

Table. 1. Spin polarization of CFAS sputtered thin films on MgO

Method	**T_g (°C)**	**T_a (°C)**	**H_c (Oe)**	**M_s (emu/cc)**	**Spin polarization (%)**
2-step	RT	-	30	690	45
2-step	RT	350	15	1190	40
2-step	RT	550	49	1170	60
2-step	RT	600	48	1230	73
1-step	600	-	125	1197	50

Tezuka et al. [24] reported that they obtained significantly lower spin polarization from CFAS with high ordered structure ($L2_1$) than less ordered structure (B2). They attributed the difference in the polarization measurements to the higher roughness of the films with $L2_1$ ordering compared to B2 [25].

A tunnel barrier is required for some of the most interesting and potentially useful spintronic devices as an active part of the device. Also, in the past, the spin injection inefficiency caused by conductivity mismatch [27] has been overcome with a tunneling [28] through an appropriate barrier. Al oxide [3, 29], MgO [2, 5, 6], and mixture of these two oxides [4] have been used as barriers. To evaluate the efficiency of electron tunneling, a key requirement for spin injection, transport from CFAS surface through tunnel barriers. I used structures with a CFAS electrode, native CFAS oxide or native AlO_x tunnel barriers and a superconducting Pb counter-electrode to perform tunneling

spectroscopy. The CFAS electrodes were prepared using the 2-step process with a 600 °C anneal temperature, since this process resulted in the highest magnetic saturation and spin polarization observed in this work. Fig. 13-a, and b show the results of measurements of tunnel junctions with native CFAS oxide and native Al oxide barriers, respectively. There is no evidence of the zero-bias resistance peak in either characteristic that arises from magnetic scattering in the barrier [30]. The peak in the BCS density of states, as reflected in the conductance-voltage characteristic, was not detected in junctions with barriers made of the native CFAS oxide, indicating a lack of direct tunneling. The observed conductance-voltage characteristic (Fig. 13-a) has a high-voltage conductance of ~0.009 Ω^{-1} with a V_{onset}, as labeled in Fig. 11-a, of ~1.8 mV. The V_{onset} value is greater than the zero-temperature lead gap value of 1.36 mV. This observation, along with the relatively small conductance and the lack of the BCS density of states peak, resembles the characteristics of Giaever-Zeller tunneling process [31] and could be caused from electron trapping in the native CFAS oxide barrier.

In contrast, the conductance-voltage characteristic for the junction with the native AlO_x barrier (Fig. 13-b) resembles that of a superconductor-insulator-metal (SIN) tunneling behavior with BCS density of states, $\frac{E}{\sqrt{E^2-\Delta^2}}$, and a superconductor gap, Δ, of 1.4 mV. To estimate the fraction of current that is transported by tunneling, the conductance minima of the structure with the AlO_x barrier was fit to a sum of an SIN characteristic and a resistive component. This analysis indicates that ~85% of the current involves tunneling. The use of a superconductor electrode with its superconductor energy gap and its BCS density of states allows us to quantitatively determine the fraction of

direct tunneling across the barrier, a process that does not involve spin flips or trapping in the barrier. It is more challenging to identify and model the non-tunneling components. To estimate the fraction from direct tunneling, the measured conductance of CFAS/AlO_x/Pb junction was fit with the sum of theoretical SIN junction and Giaever-Zeller like conductance characteristics. At 4.2 K the best fit comes when the ideal SIN conductance take 50% (±10%) of the weight ratio (Fig. 13–c). Additional optimization of the tunnel barrier is expected to improve this factor. Nevertheless, these results clearly show that an AlO_x barrier can serve as a useful direct tunnel barrier.

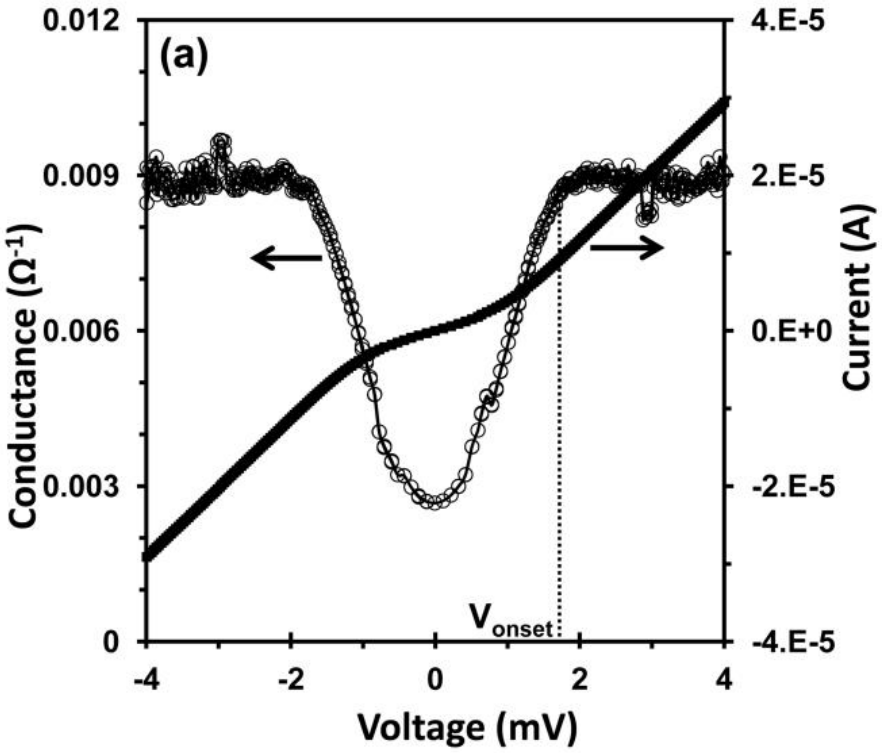

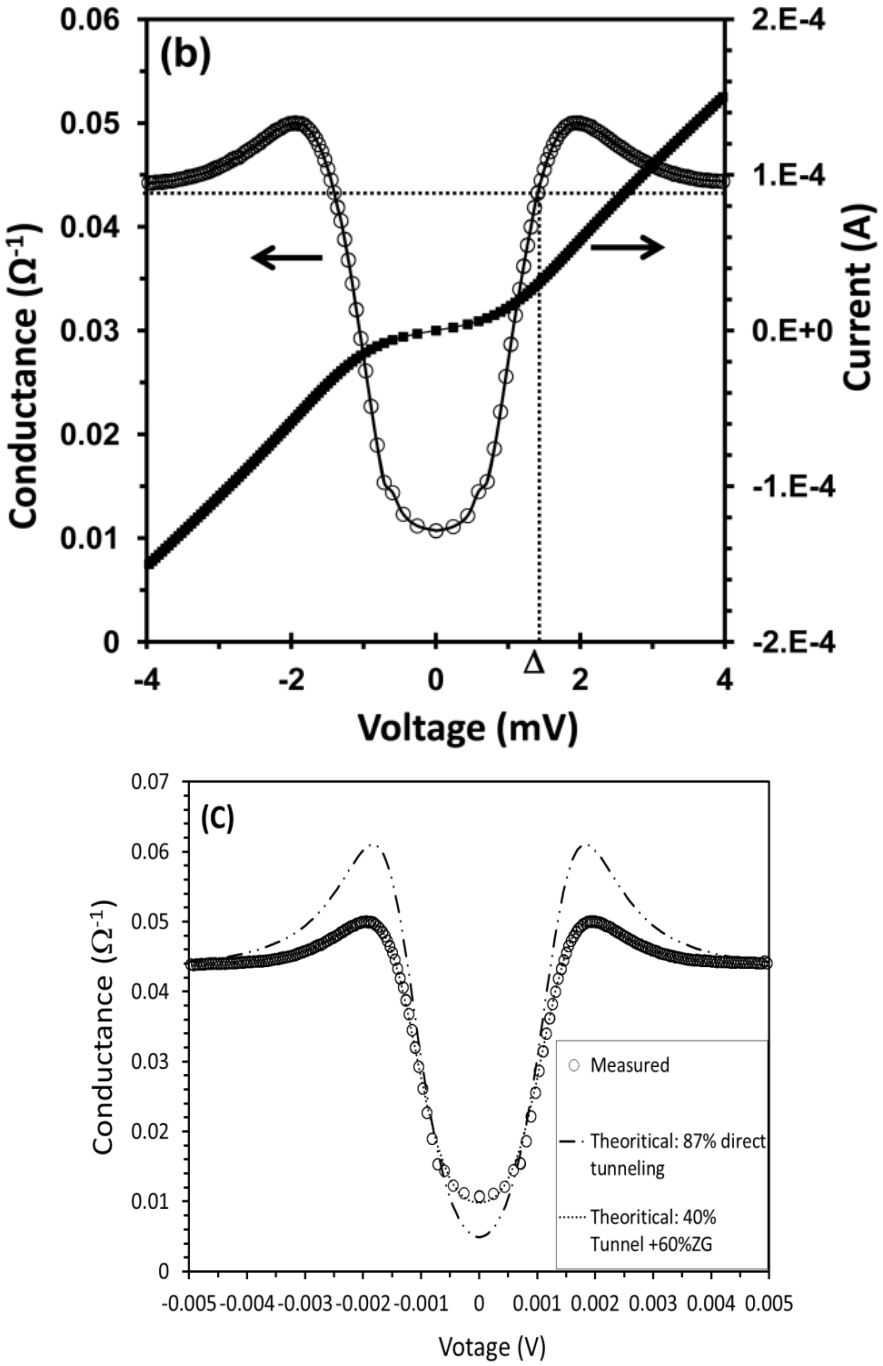

Fig. 13. Results of tunnel junction measurement of superconducting CFAS/barrier/Pb at 4.2 K, with a) natural oxide, b) native Al oxide as a barrier layer, and c) theoretical calculation for junction with Al oxide barrier.

As an alternate growth method, I used PLD to prepare CFAS thin films at RT and then annealed them in-situ. Fig. 14 shows a comparison between magnetic properties of

films prepared with PLD and those prepared by sputtering. From the figure it can be concluded that the magnetic properties of sputtered CFAS films are better than films prepared by PLD, since H_c is the same but M_s is smaller. However, the spin polarization values measured for films prepared by PLD were equal to those for films prepared by sputtering, Table. 2.

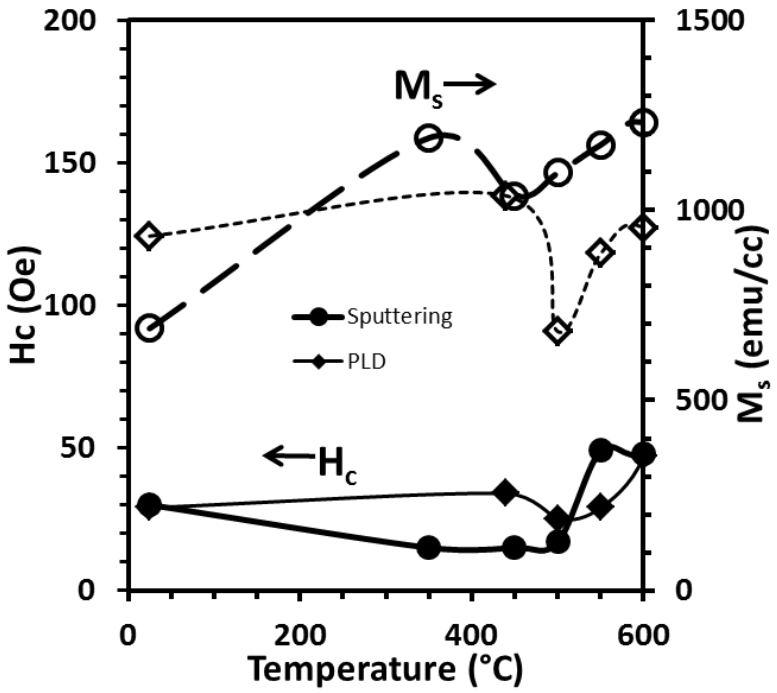

Fig. 14. Comparison of magnetic properties of 2-step-processed samples prepared by PLD and sputtering.

Table. 2. Spin polarization of CFAS thin films grown on MgO at RT and annealed at 550 °C

Processing method	**H_c (Oe)**	**M_s (emu/cc)**	**Spin polarization (%)**
Sputtering	49	1170	60
PLD	29	890	60

2.4. Conclusions

CFAS thin films were synthesized and characterized with different growth methods and under different growth conditions. Highly ordered $L2_1$ structure of CFAS films was achieved by growing films in 1-step procedure at substrate temperatures of more than 450 °C. CFAS thin films sputtered using either a 2-step and 1-step process exhibited excellent magnetic properties. The spin polarization at the surface of these thin films was investigated as a function of growth conditions with the PCAR method. The largest value for spin polarization was measured to be 73%. AlOx oxide barriers exhibited a high fraction of direct tunneling (> 50%) while native CFAS oxide did not show any direct tunneling. In both cases, transport was through the oxide and not through pinholes or other high transparency regions.

Chapter 3

DETERMINING OPTIMAL GROWTH CONDITIONS FOR $ZnGeAs_2$ THIN FILMS, CONSISTS OF EARTH ABUNDANT ELEMENTS, FOR PHOTOVOLTAIC APPLICATIONS

3.1. Introduction

$ZnGeAs_2$ is a semiconductor comprised of only inexpensive and earth-abundant elements [8]. $ZnGeAs_2$ films with hole mobilities of greater than 50 $cm^2/V \cdot sec$ [9-11] and minority carrier lifetimes of ~150 ns [12] have been reported. These observations, in conjunction with the natural abundance of their constituents, suggest that this material is a good candidate to make low-cost, efficient photovoltaic cells. Furthermore, $ZnGeAs_2$, in combination with $ZnSnP_2$, could potentially be useful for producing tandem solar cells because they are lattice matched and have direct bandgaps of 1.15 eV and 1.65 eV, respectively [33].

However, there are limited $ZnGeAs_2$-based thin-film devices fabricated at the high temperatures, required to attain epitaxially-grown $ZnGeAs_2$ thin-films, due to the challenge of incorporating volatile Zn and As species into the growing films at elevated temperatures. As an example, Chelluri et al. [10] used molecular beam epitaxy (MBE) to grow single crystalline Ge-$ZnGeAs_2$ alloy films at a substrate temperature of 380 ^oC with very high Zn:Ge and As:Ge flux ratios. In another study, Shah and Greene [9] sputtered single crystal $ZnGeAs_2$ thin films at a substrate temperature of 450-520 ^oC, using a $ZnGeAs_2$ target with the Zn and As_4 overpressure of 1 mTorr evaporating from Knudsen

cells. In those studies, less than 1% of the Zn and As atoms, impinged the deposition surface, were incorporated into the deposited films.

In order to achieve high quality $ZnGeAs_2$ films, precise control of the growth conditions is essential. Solomon et al. [11] and Timmons et al. [12] found that a 30 ^oC shift in the $ZnGeAs_2$ growth temperature during OMVPE (organometallic vapor phase epitaxy) synthesis resulted in significant differences in the film's composition and structure. By comparison, GaAs can be grown by MBE at temperatures ranging from 500 to 800 ^oC at As_4 overpressures in the range of 10^{-6} to 10^{-4} Torr [32].

Thermochemical analysis can be used to predict optimal conditions for attaining high quality epitaxial growth. The optimal growth conditions, in other semiconductor systems, can be attained using the substrate growth temperature typically in the range of one-half to two-thirds of the melting temperature on the absolute scale (i.e., K) of the material [33]. At lower temperature the incident atoms do not have enough thermal energy to overcome the kinetic barriers for surface diffusion, nucleation, and incorporation into the lattice, and the resultant films are generally amorphous. PLD deposited films of $ZnGeAs_2$ follow this trend, as XRD spectra indicates as-deposited films are amorphous at substrate temperatures up to 588 K. These temperatures are far below the melting point of $ZnGeAs_2$, reported as 1128 K [34], and the calorimetrically determined crystallization temperature of 733 K [9]. The epitaxial growth temperature of $ZnGeAs_2$ on GaAs was 653 K for MBE [10], 723-793 K for sputtering plus Zn and As_4 co-evaporation [9], and 853 K for OMVPE [11]. OMVPE requires this relatively high temperature to crack GeH_4 source.

To better understand the rate limiting step involved in $ZnGeAs_2$ film growth, I studied the thermodynamic and kinetic factors associated with the growth process.

3.2. Experimental procedure

$ZnGeAs_2$ thin films were grown by PLD in a UHV chamber with base pressure below 5×10^{-7} Torr. Films were deposited with two flux rates, by operating a 248 nm KrF excimer pulsed laser at either 5 or 10 Hz with an energy of 450 mJ/pulse. The argon gas pressure during deposition was maintained at 400 mTorr. The distance from target to substrate was fixed at ~5 cm. A stoichiometric polycrystalline $ZnGeAs_2$ target was made from Zn, Ge and As (99.9999% pure, Alfa Aesar) and reacted in an evacuated quartz ampoule at 1000 ^{o}C for 24 hours. Particle-induced X-ray emission (PIXE) measurements demonstrated that the target is stoichiometric. XRD measurements showed a single phase chalcopyrite structure $ZnGeAs_2$ in the target material. A Zn-enriched target with a nominal composition of $Zn_{1.4}GeAs_2$ was also synthesized in order to study the effect of higher relative Zn impingement rates on the composition of thin films. Composition and thickness of the thin films were inferred using RBS measurements and analysis. Structural characterization was performed using high resolution XRD.

Measurements of the thermal decomposition rate of $ZnGeAs_2$ polycrystalline bulk samples were performed in the same UHV chamber. The heating rate was adjusted to ~15 ^{o}C /min. The residual gas analyzer (Stanford Research System, model RGA300) was located ~25 cm away from the sample. Vapor pressure of each volatile species during decomposition was monitored in-situ by the RGA. The composition of the bulk sample

was analyzed before and after decomposition using RBS and energy dispersive spectroscopy (EDS).

Since the thermodynamic Ellingham diagrams for $ZnGeAs_2$(s) have not been experimentally determined, the equilibrium vapor pressure over ZGA as a function of temperature was calculated from first principles using total energy calculations and applying Density Functional Theory (DFT) with the local density approximation (LDA) [35], and also the Perdew-Burke-Ernzerhof (PBE) [36] functional, since the LDA is known to systematically overbind. Total energy calculations were performed to calculate the vacancy formation energy of the three atomic species. The defect super cell was relaxed using the full-potential (FP) linearized muffin-tin orbital (LMTO) method [37]. After calculation of the reference ZGA cell and the three defect cells total energies, the defect formation energies were calculated following Zhang et al. [38]. Then, to calculate the equilibrium vapor pressure, a statistical mechanics approach was taken, where partition functions for the various components (e.g. solid and gas species) were constructed. These partition functions were used in the minimization of the system's free energy with respect to the number of gas phase atoms. When this is used with the ideal gas law, it gives the equilibrium vapor pressure of the system. To simplify the system, it was assumed that the gas phase must have the same stoichiometry as the solid phase.

3.3. Results and discussion

Fig. 14 [39] schematically represents various contributions to the deposition-decomposition process and depicts the terms for the element-specific rates that are used

here: The deposition rate is defined as the total number of atoms deposited per unit time and area. The decomposition rate is the atomic loss evaporated from a fully reacted compound per unit time and area (Fig. 15). The incorporation rate is defined as the total numbers of atoms that react to form the fully reacted compound per unit time and area. The adsorption rate (or precursor evaporation rate) is the number of atoms in precursor form (i.e. that are not fully reacted into the bulk $ZnGeA_2$ phase) re-evaporated from the substrate per unit time and area.

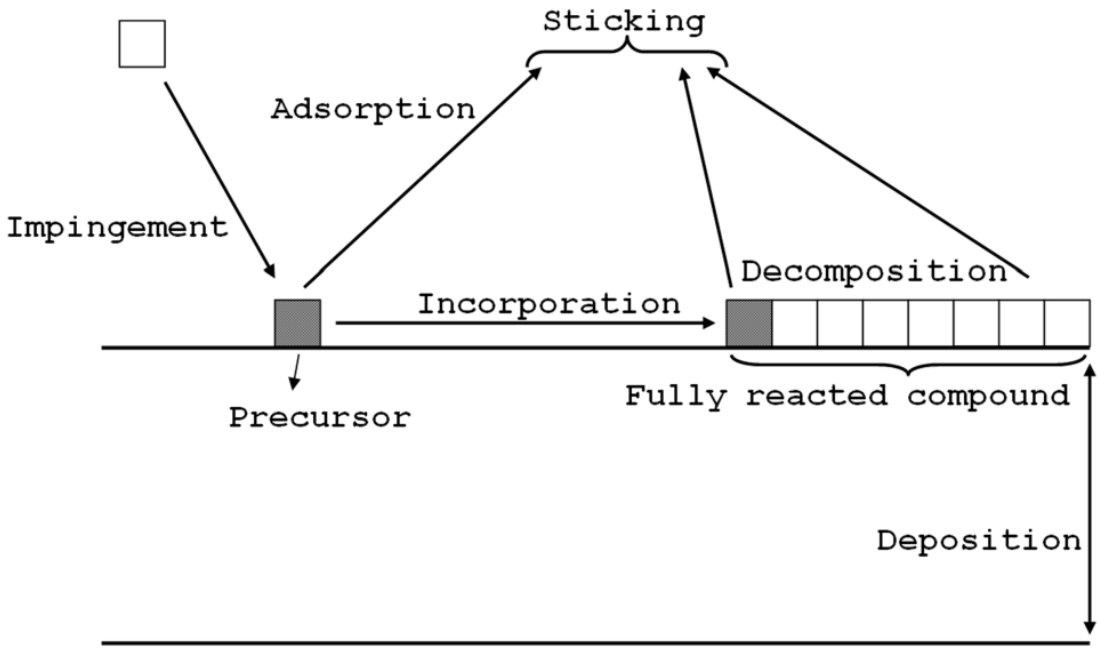

Fig. 15. Schematic representation of impingement, adsorption, decomposition, sticking, incorporation, and deposition rate definitions used in this study.

According to the previous study [10], it was shown that within the temperature range of this study, Ge has a near-unity sticking coefficient. By using this assumption and the knowledge of the target stoichiometry, the effect of run-to-run variations in the reactant impingement rates, resulting from changes in laser power and/or the target

condition, can be corrected by plotting the relative number of deposited Zn and As atoms with respect to Ge, as shown in Fig. 16-a, and b. The composition of films grown from the stoichiometric target was found to vary significantly with substrate temperature, as summarized in Fig. 16-a. For substrate temperatures below 275 ^{o}C, the composition of the films grown with 10 Hz laser frequency is similar to that of the target. For temperatures higher than 275 ^{o}C, the films are Zn- and As-deficient. At 400 ^{o}C, the deposited film is predominantly Ge with only a few percent of Zn and As.

Although the high energy density of the laser beam is known to congruently ablate target material [40], differences between the stoichiometry of the target and films are often encountered when the material contains highly volatile species as a result of finite rates of adsorption and/or decomposition. For instance, Li-deficiency is generally observed in $LiNbO_3$ [41] and Zn-deficiency in $Ba(Zn_{1/3}Ta_{2/3})O_3$ [40] when thin films are deposited at the elevated temperatures required to achieve high-quality epitaxy.

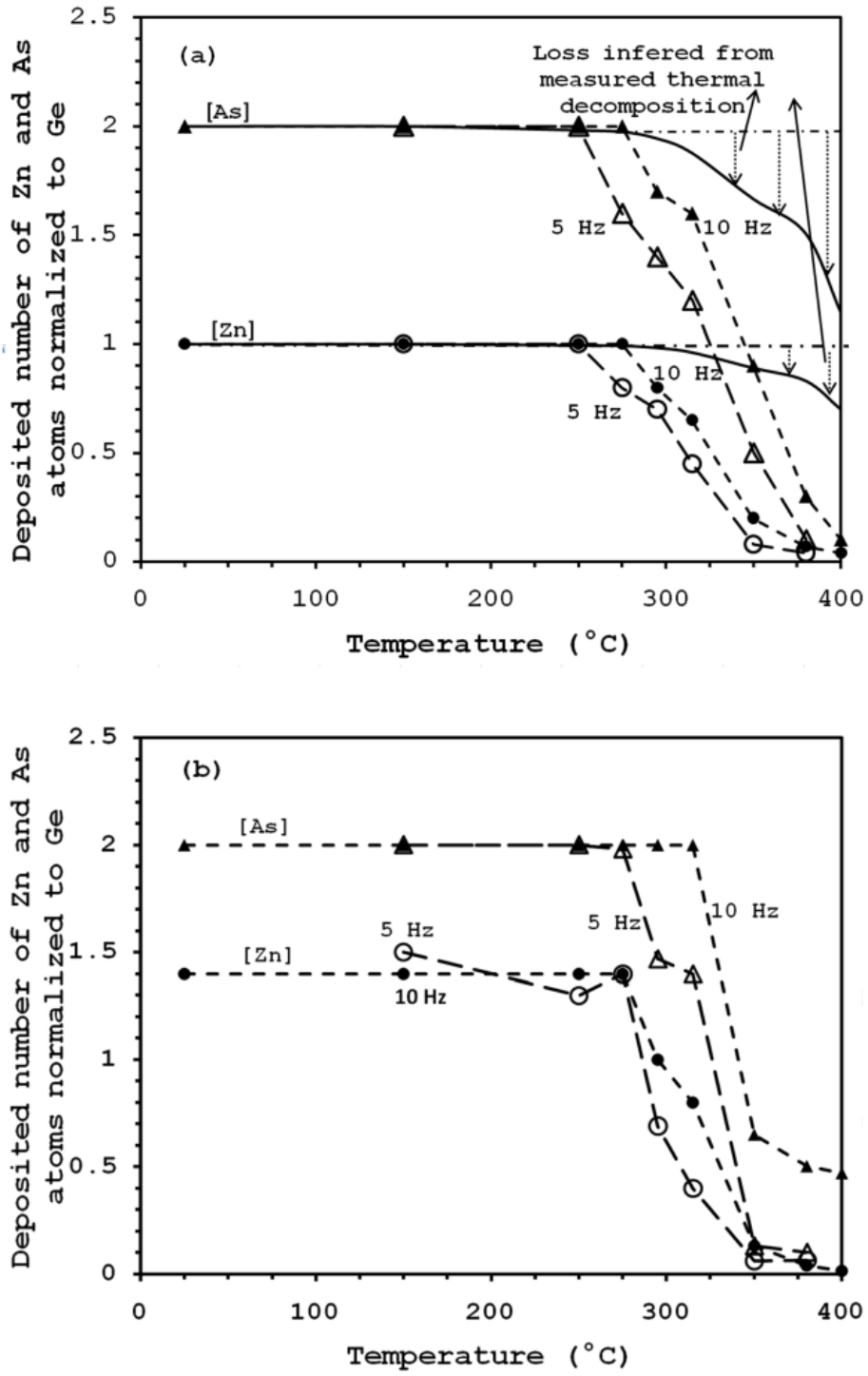

Fig. 16. The normalized number of Zn and As atoms with respect to Ge deposited in thin films grown by pulsed laser deposition of a) stoichiometric $ZnGeAs_2$ target and b) Zn-enriched $Zn_{1.4}GeAs_2$ target inferred from RBS measurements and analysis. Deposited

number of atoms for each reactant is defined as the total number of atoms accrued in the film per unit area, calculated from RBS data. In figure (a), the dashed arrows illustrate the amount of Zn and As that would be lost based on the measured thermal decomposition rate alone.

To perform experiments with the same net deposition but at different rates, the laser frequency was changed from 10 to 5 Hz and the deposition time was doubled. In this way one can distinguish between the sticking coefficient (which is determined by the efficiency of incorporation from the precursor state into the fully reacted compound, and does not depend on deposition duration) and thermal decomposition (which is determined solely by the properties of the fully reacted compound, is constant with time and therefore does depend on the deposition duration). If the total number of deposited atoms is the same for these two conditions, the process is determined exclusively by the sticking coefficient; differences can be attributed to the thermal decomposition. The results of these experiments are shown in Fig. 16-a.

There is a large and systematic difference between the fast and slow deposition for temperatures above 275 °C, and it is concluded that thermal decomposition plays an important role in the process for these temperatures. The equation $\mathrm{Fr}_{\mathrm{decomposition}} = \frac{D_{10}-D_5}{D_{10}-D_{nl}}$ was used to determine the fraction of Zn and As atoms lost as a result of decomposition compared to the total loss at each temperature. In the equation D_{10}, D_5 and D_{nl} refer to the deposition ratio attained from growths at 10 Hz, at 5Hz and for the condition assuming no loss (i.e. for constant stoichiometry as shown by the horizontal line in Fig. 16-a), respectively. If the fraction equals one, then the losses arise from decomposition alone, while if it is zero then the losses are entirely from adsorption. The loss is small for growths below ~295 °C. For growths with a substrate temperature

ranging from 295 to 315 °C, the $Fr_{decomposition}$ obtained are 1.0±0.1 for As loss, indicating that decomposition dominates for this species, and 0.5±0.1 for Zn loss, indicating that decomposition and adsorption plays a nearly equal role. The significance of the kinetically-limited thermal decomposition, as shown in Fig. 16-a, will be described after discussing Fig. 17.

As a route to increase the maximum growth temperature that retains the ideal ($ZnGeAs_2$) stoichiometry of deposited films, a Zn-enriched target with nominal composition $Zn_{1.4}GeAs_2$ was also used. The normalized number of atoms deposited for each element with respect to Ge for the Zn-enriched target is presented in Fig. 15-b. As the figures show, the maximum growth temperature that can attain stoichiometric $ZnGeAs_2$ films was not significantly increased by the use of the Zn-enriched target.

An investigation to determine the $ZnGeAs_2$ decomposition rate was performed to allow for quantitative analysis of the thermochemistry of $ZnGeAs_2$ thin film growth. Fig. 16 illustrates the Arrhenius plots of the Zn and As_2 measured dissociation vapor pressures as a function of substrate temperature. The theoretically-determined thermodynamic Zn and As equilibrium pressure over a $ZnGeAs_2$ phase is also presented in Fig. 16. An experimental measurement of the overpressure at the melt temperature is found to show excellent agreement with the theoretical prediction [42]. As illustrated in Fig. 15, the dissociation vapor pressures of Zn and As are two-to-four orders of magnitude lower than the thermodynamic equilibrium pressure at corresponding temperatures. This demonstrates that the decomposition rate is kinetically limited with an evaporation

coefficient of 10^{-4} to 10^{-2}. Large kinetic barriers to decomposition are also found in strongly bound materials such as GaN [43, 45], AlN [46], diamond [47], and MgB_2 [48].

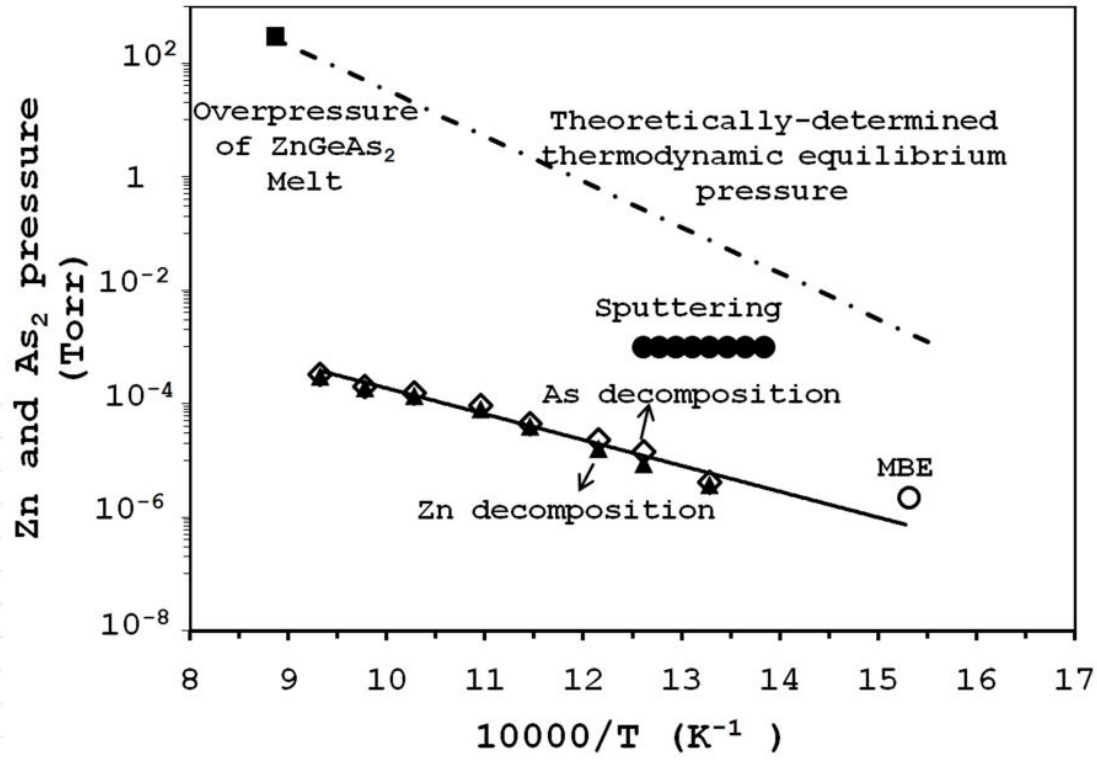

Fig. 17. An Arrhenius plot of the Zn and As dissociation vapor pressure during $ZnGeAs_2$ decomposition. Theoretically-determined thermodynamic Zn and As equilibrium pressure over a $ZnGeAs_2$ phase. Also included in the figure are the Zn and As pressure used during $ZnGeAs_2$ growth by sputtering [9] and MBE [10], and the pressure measured over a $ZnGeAs_2$ melt [42].

In this study, the Zn and As evaporation rates reached one monolayer per second (~10^{-6} Torr) when the $ZnGeAs_2$ temperature was 425 ^{o}C, as illustrated in Fig. 17. The activation energy of $ZnGeAs_2$ decomposition is 1.08±0.05 eV. During the decomposition process, the Zn/As_2 pressure ratio is very close to unity, suggesting that when either Zn or As dissociates from the $ZnGeAs_2$, the other tends to immediately evaporate. Therefore, it

is concluded that the kinetically-limited decomposition reaction is: $ZnGeAs_2(s) \rightarrow Ge\ (s) + Zn\ (v) + As_2\ (v)$.

Fig. 17, also, includes data from the Zn and As pressure used during sputter deposition of epitaxial $ZnGeAs_2$ by Shah and Greene [9] and MBE by Chelluri et al. [10]. Since the Zn and As partial pressures fall between the predicted thermodynamic equilibrium rate and the measured kinetically limited decomposition rate, it can be inferred that both sputtering and MBE $ZnGeAs_2$ growth are in the metastable regime.

Next, the relative role of thermal decomposition in determining the film deposition rate and stoichiometry is analyzed. This will allow comparison between the thermal decomposition rate measured in this study (performed in vacuum), which is a lower bound to the reverse reaction, and the decomposition rate during plasma-assisted growth. It is well known that the impinging energetic atomic and molecular species can affect decomposition rate, and this process has been termed "thermally assisted sputtering" or "sputtering enhanced decomposition". Fig. 16-a illustrates the inferred deposition of Zn and As atoms in films grown at the 10 Hz laser frequency assuming a sticking coefficient of unity for all reactant atoms (i.e. formation of fully reacted $ZnGeAs_2$ compound) and the thermal decomposition. It is clear that the observed decomposition as inferred from the Zn and As loss during growths is higher than expected from $ZnGeAs_2$ thermal decomposition alone. The difference between these values can be attributed to the effect of plasma enhanced decomposition. Fan et al. [48] showed that the bombardment of large kinetic ions (at 70 eV) in the nitrogen plasma

increases the decomposition rate of AlN by a factor of ~2. In comparison, during PLD growth the depositing species have kinetic energies of 10–100 eV [49].

Thus far, it has been shown that high quality $ZnGeAs_2$ film growth can be attained in the metastable regime if the incident volatile elements flux rate (i.e., Zn and As) is high enough to compensate the decomposition losses of these elements. Therefore, Fig. 17 can be used to predict the maximum substrate temperature where stoichiometric growth can be expected as a function of reactant impingement rate. For example, a $ZnGeAs_2$ growth of 1 μm/hour at 450 ^{o}C requires a Ge flux density of > $3x10^{14}$ atoms·cm^{-2}·sec^{-1}, or ~$2x10^{-6}$ Torr beam-equivalent-pressure, based on the deposition of reactants and $ZnGeAs_2$ decomposition experimental data. The Zn and As flux density should then be at least 10^{16} atoms·cm^{-2}·sec^{-1}, or >$7x10^{-5}$ Torr beam-equivalent-pressure, to negate the decomposition loss during high temperature growth.

So far it is found that to attain high quality epitaxial $ZnGeAs_2$ growth with vapor phase deposition techniques, high substrate temperatures and large Zn and As fluxes are vital. As an alternative method, high quality $ZnGeAs_2$ films can be achieved by deposition of amorphous films at low temperature followed by a high temperature annealing to crystallize the films. The decomposition study indicated that ~10^4 monolayers of $ZnGeAs_2$ (or ~3 μm thickness) would be evaporated for anneals at 600 °C for 300 s, so an SiO_2 capping layer was deposited on the film to minimize this process. This annealing procedure produced textured films with X-ray diffraction rocking curve width of less than 80 arc-minutes, Hall carrier concentrations as low as $5x10^{17}/cm^3$ and mobilities greater than 50 $cm^2/V{\cdot}s$.

3.4. Conclusions

The $ZnGeAs_2$ PLD growth and thermal decomposition studies showed that the substrate temperature needed to achieve high-quality $ZnGeAs_2$ epitaxy is largely determined by the kinetic barrier to decomposition. Due to this large kinetic barrier to decomposition with an evaporation coefficient of 10^{-4}-10^{-2}, high quality films can be grown in the metastable regime. It is noteworthy that compounds with small evaporation coefficients, as a result of kinetically-limited decomposition reaction including $ZnGeAs_2$, GaN, AlN, diamond and MgB_2, can all be synthesized by vapor phase methods under metastable condition.

Chapter 4

SYNTHESIS AND CHARACTERIZATION OF PYRITE (FES_2) THIN FILMS, AN EARTH ABUNDANT COMPOUND, FOR PHOTOVOLTAIC APPLICATIONS

4.1. Introduction

Another prospective material for low cost, earth abundant photovoltaic materials is pyrite (FeS_2). Pyrite, the most abundant sulfide at Earth's surface [7], is a nontoxic semiconductor with a band gap of 0.95 eV [13], and an absorption coefficient in the visible range of 6.5×10^5 cm^{-1}, which is two orders of magnitude higher than Si [14]. Thus, it is a suitable candidate for photovoltaic applications [7, 13, 14, 50]. When cost and natural abundance of the elemental components are considered, pyrite is significantly more attractive than any other compound [51].

Synthesizing high-quality pyrite thin films is challenging, largely due to the high S vapor pressure required during the process. Previous publications have described techniques such as chemical vapor transport, CVT [52], metal organic chemical vapor deposition, MOCVD [13, 14, 52], sputtering [50, 53], MBE [54], or thermal sulfidation of iron [55, 56] and iron oxide [57] to synthesize pyrite thin films. Films grown at too low temperature have poor structural and electrical quality [54], since; at low temperature the incident atoms do not have enough thermal energy to overcome the kinetic barriers for surface diffusion, nucleation, and incorporation into the lattice. In the opposite extreme, growing at higher temperatures often resulted in S-deficient [14, 50], non-stoichiometric films. I designed, tested and operated a layer-by-layer growth technique

that produces high-quality, high-purity pyrite thin films using sequential evaporation of Fe under high vacuum followed by sulfidation at pressures >1 mTorr. The results are compared with those obtained using traditional MBE growth.

4.2. Experimental Methods

I designed and assembled a UHV chamber based on the MBE concept, schematically shown in Fig. 18, to co-evaporate Fe and S with a capability of reaching S pressures up to 10 Torr. Pyrite thin films were grown by co-evaporation of Fe and S in that chamber with a base pressure below 2×10^{-7} Torr. An alumina coated W crucible was used to thermally evaporate Fe, and an alumina crucible wrapped with W wire was used to evaporate S. The pressure of S was adjusted by controlling the crucible temperature. To measure the temperature of the S crucible (i.e., S pressure) during growth a type K thermocouple was used. Fe shot (99.98% pure, Alfa Aesar) and S particles (99.999% pure, Alfa Aesar) were used as precursors for evaporation. PIXE measurements indicated no impurities in the Fe shot above the detection limit of 100 ppm.

An ex-situ S-annealing experiment was performed to study the conditions required to convert S-deficient phases to pyrite. Two types of films were used for the annealing study; S deficient ($Fe_{1-x}S$ with $x<0.5$) films deposited by co-evaporation of Fe and S, and pure Fe films grown at RT by thermal evaporation of Fe. The desired pressure during the anneals was attained by inserting the precise amount of S into the sealed tubes for the chosen annealing temperature. Then samples were sealed in evacuated quartz ampoules. Finally, the samples were heated in a tube furnace at 350 to 500 °C for 1.5 hr.

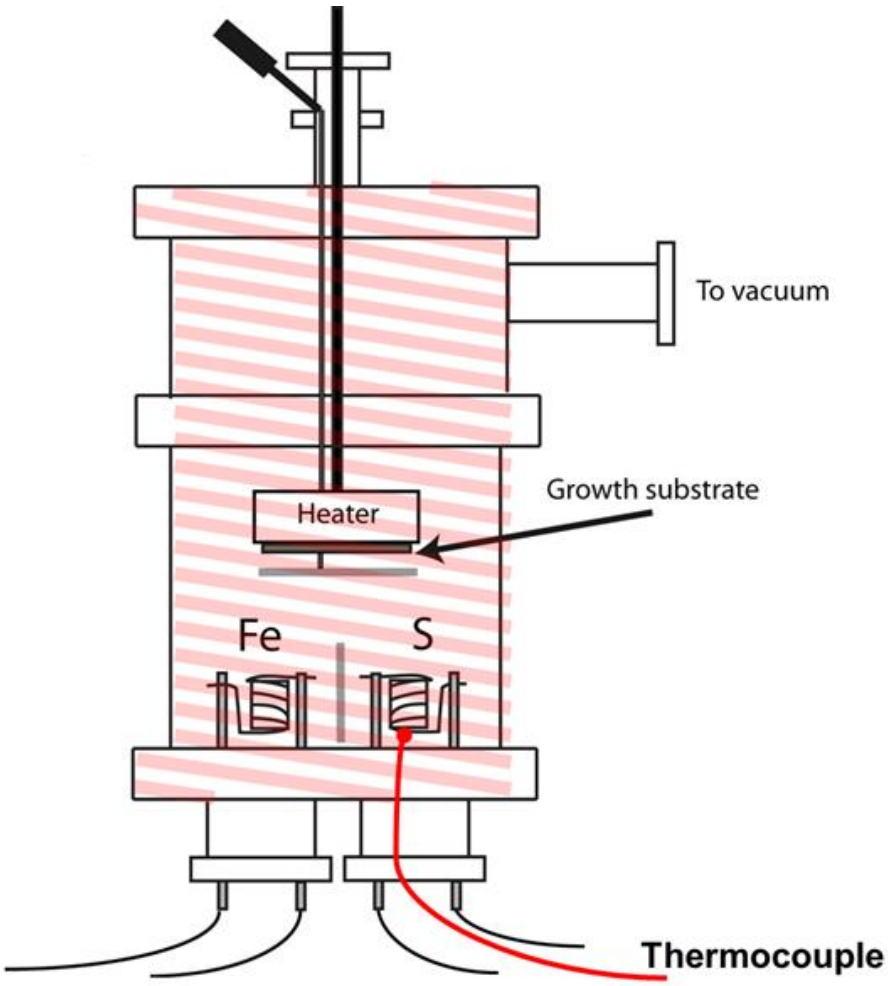

Fig. 18. Schematic of MBE type UHV chamber to perform high sulfur pressure co-evaporation of Fe and S.

For the sequential evaporation method the heated substrate rotates between a low-pressure Fe evaporation zone and a high-pressure S evaporation zone (Fig. 19), similar to the pocket heater developed by Kinder [58] and used by others [59]. Fe evaporation is performed in the unbaked UHV chamber with a base pressure $<1.5\times10^{-5}$ Torr, where most of the background pressure is S vapor. The S pressure inside the S evaporation zone is maintained between 1 mTorr and 1 Torr. A pressure difference of greater than three

orders of magnitude between the Fe and S deposition zones can be achieved. The rotation speed was fixed at ~4.5 rpm.

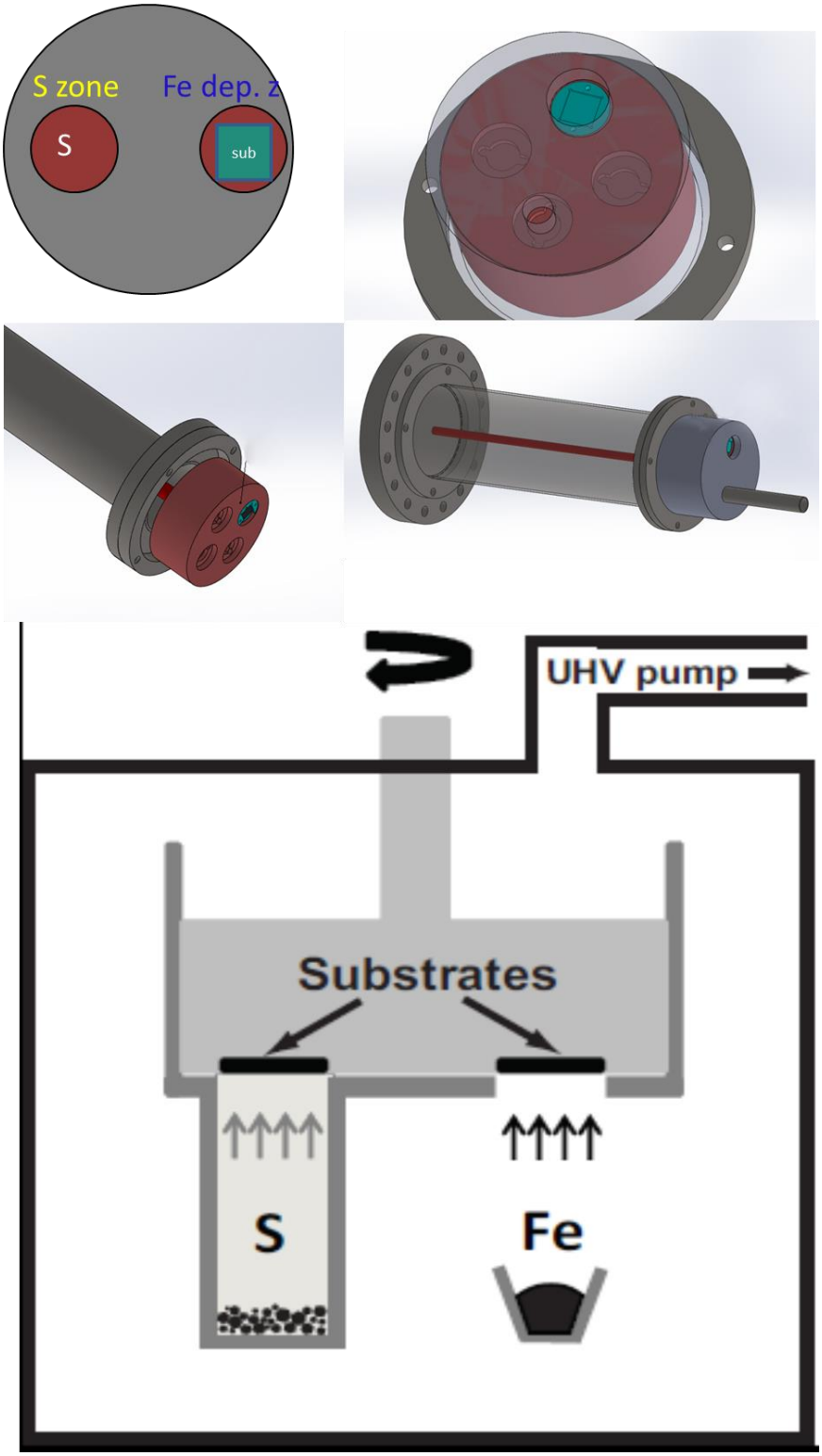

Fig. 19. Schematic of the device designed for sequential evaporation of Fe and S to deposit pyrite thin films with layer-by-layer growth.

The stoichiometry and thickness of the thin films was inferred from RBS measurements and analysis. EDX, SIMS, and PIXE were used to validate the conclusions from the RBS analysis and monitor the trace contaminants. Structural characterization was performed using XRD. The Raman laser was operated with less than 5 mW of 532-nm laser excitation to prevent decomposition at the surface from heating effects. Scanning electron microscopy (SEM) and transmission electron microscopy (TEM) were used to study the structural and chemical properties of the thin films. An aberration-corrected 200 kV JEOL ARM scanning TEM (STEM) was used for atomic-scale imaging and chemical analysis. Other microscopes used for TEM imaging included JEOL 4000 EX 400 kV and JEOL 2000, 200 kV instruments. The resistivity was measured using a 4-point probe in the van der Pauw configuration.

4.3. Results and discussion

I adopted the Fe-S phase diagram from Waldner and Pelton [60] and designed the Fe, S co-evaporation and ex-situ annealing experiments to cover the area shown in Fig. 20, by changing S pressure, substrate temperature, and annealing temperature. The initial pyrite films were deposited by co-evaporation of Fe and S followed by cooling down in-situ in vacuum to RT. RBS results from these experiments are summarized in Fig. 21-a, and b. As can be seen, films grown at substrate temperatures higher than 100 °C are S deficient, similar to the MBE growth results of Bronold et al. [54]. In addition, growth over a wide range of S pressures at 350 °C substrate temperature also produced S-deficient films (Fig. 21-b). Presumably kinetic factors play a role in producing S-deficient films under these conditions since pyrite is the stable phase at 1 Torr and temperatures up

to ~550 °C (Fig. 20). The effect of substrate temperature on the morphology of deposited thin films is shown in Fig. 22. SEM images of films, deposited at 1 torr of S pressure at different substrate temperatures, indicate that films are rougher and more granular at higher growth temperatures.

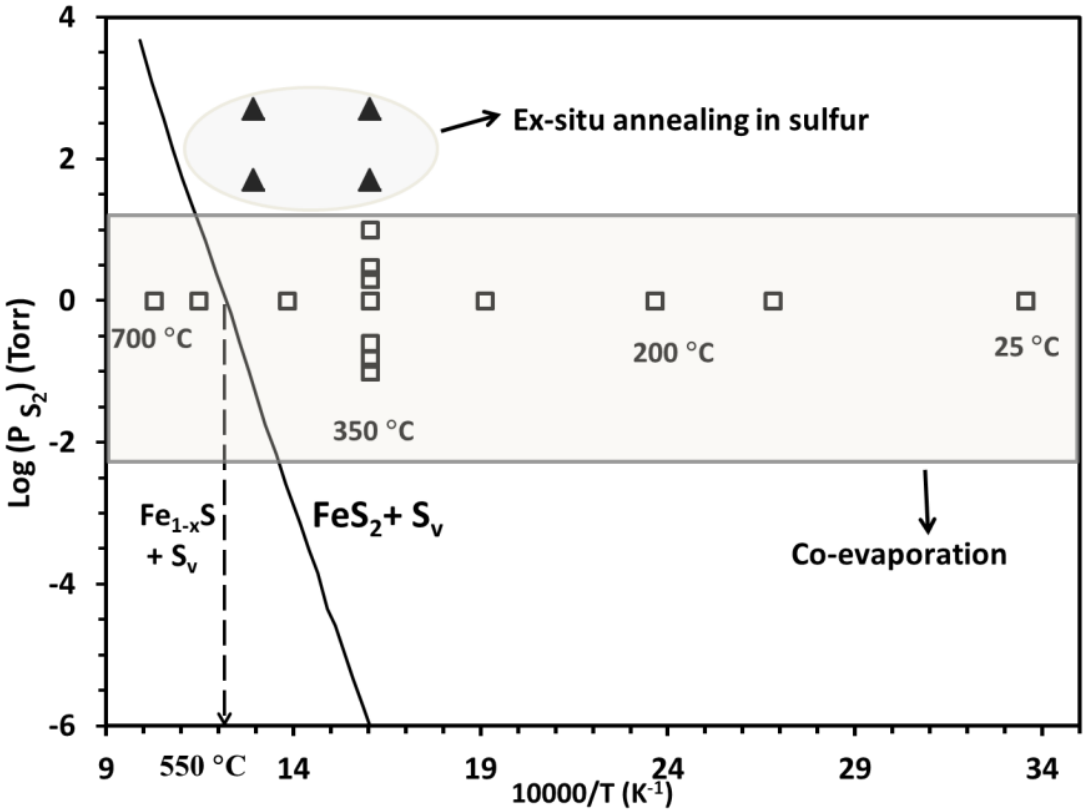

Fig. 20. Fe-S phase diagram constructed from Waldner and Pelton [60] showing the area explored by co-evaporation of Fe and S, and the ex-situ annealing experiments.

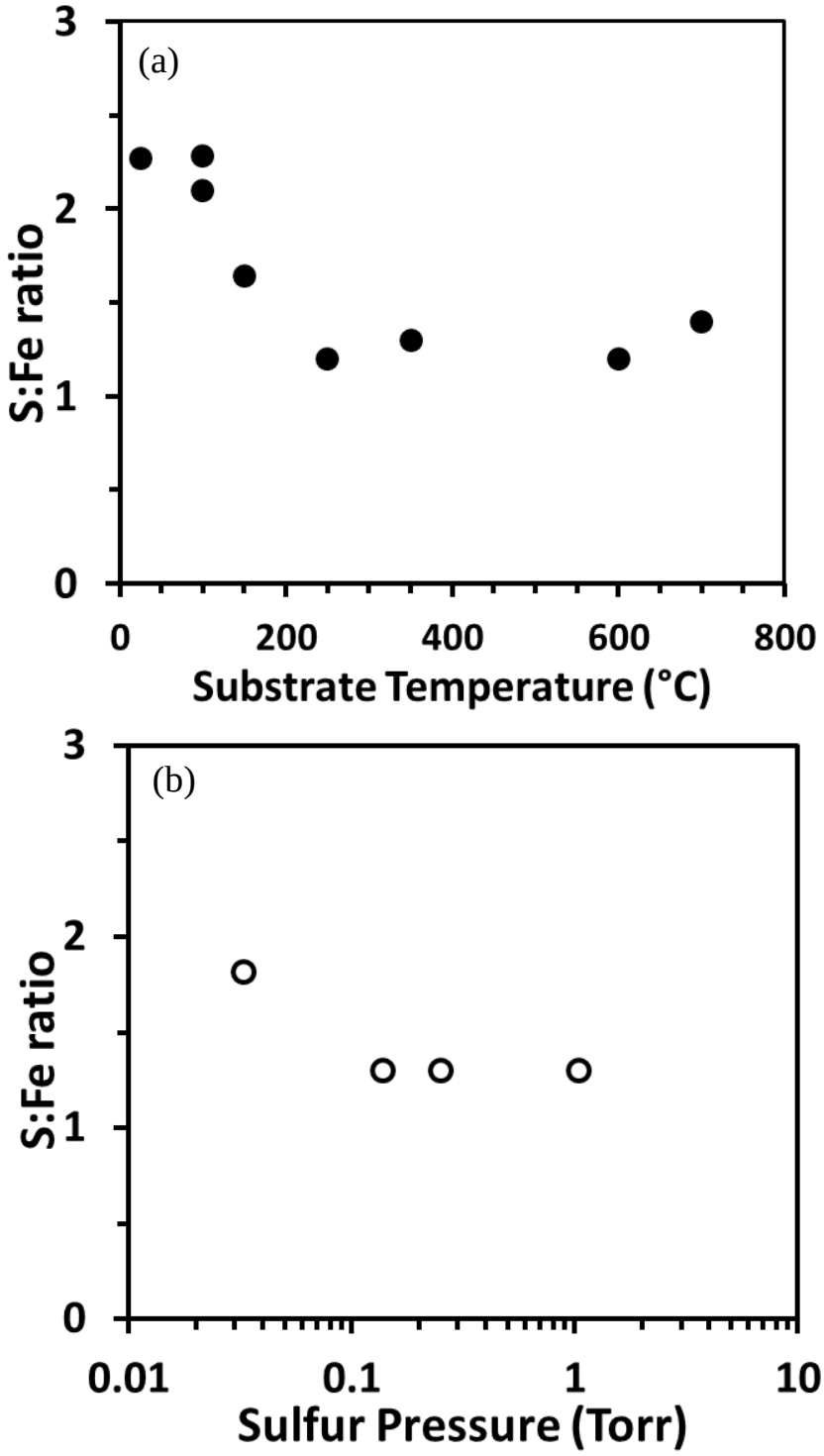

Fig. 21. Pyrite thin films grown at a) different substrate temperatures at P_s=1 Torr, b) at different S pressures at substrate temperature of 350 °C. All films were cooled in vacuum after growth.

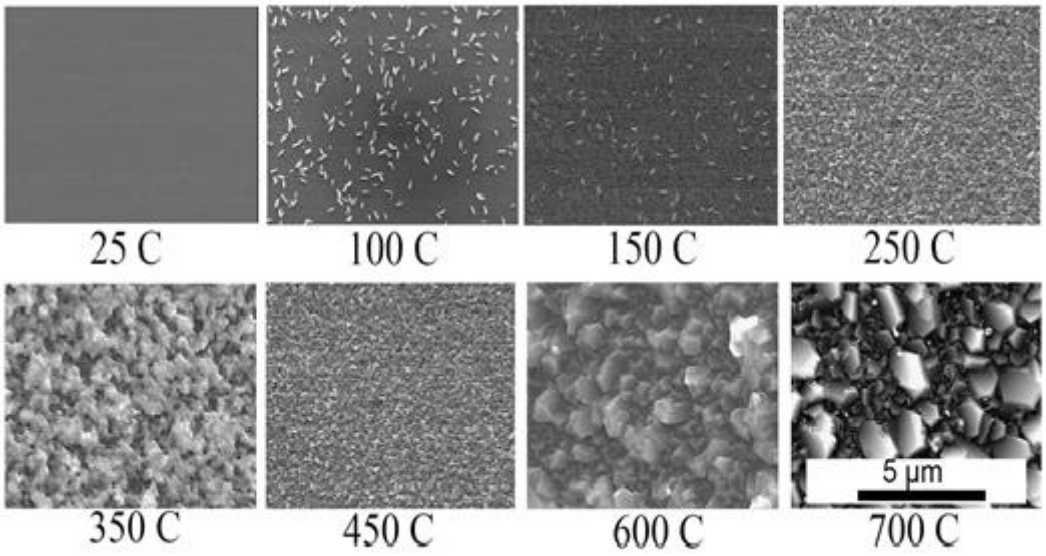

Fig. 22. SEM images of films deposited by co-evaporation of Fe and S at 1 Torr of S pressure and different substrate temperatures.

Single-phase pyrite was not produced by co-evaporation of Fe and S followed by cooling in vacuum, even when S pressures of 1 Torr were used. However, stoichiometric pyrite was produced during cool-down from the growth temperatures in a S rich environment. In an effort to prevent any S loss during cooling, the as-deposited films obtained by co-evaporation were cooled to 100 °C in P_s=1 Torr from their growth temperatures. Then, to remove the excess S, the samples were annealed in-situ at 180 °C for three minutes. For films grown at 350 °C and a S pressure of 1 Torr, the average S:Fe ratio increased from ~1.3:1 to an average value of ~1.9:1 when the films were cooled in 1 Torr S pressure as opposed to vacuum . The XRD spectrum from the latter film (Fig. 23-a) is comparable to that of the MBE-grown pyrite film deposited on a 120 °C substrate and reported by Bronold et al. [54] (Fig. 23-b).

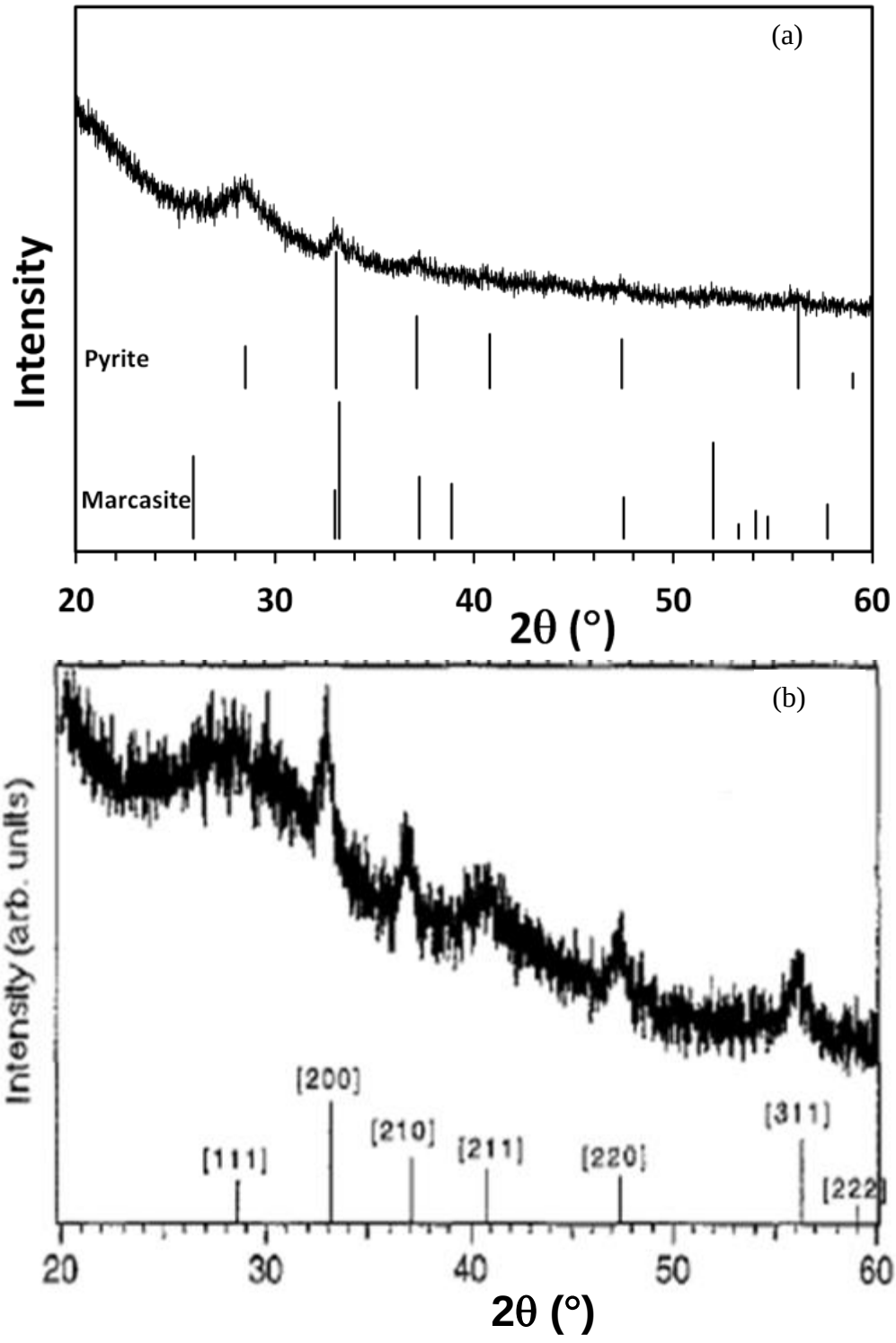

Fig. 23. XRD results of, a) film grown at $T_{substrate}$= 350 °C by co-evaporation of Fe and S at P_s=1 Torr followed by cooling down in 1 Torr S pressure, b) MBE grown pyrite at 120 °C [38].

However, TEM analysis of the film showed two distinct regions. That nearest the substrate is comprised of a 125-nm layer of pyrrhotite ($Fe_{1-x}S$), which is covered by a 25-nm layer of pyrite that presumably formed during post-growth cooling (Fig. 24-a, and b). This observation shows that to form pyrite either a lower temperature or higher S pressure, or both is needed, presumably as a result of a kinetic barrier to formation of pyrite from Fe or pyrrhotite.

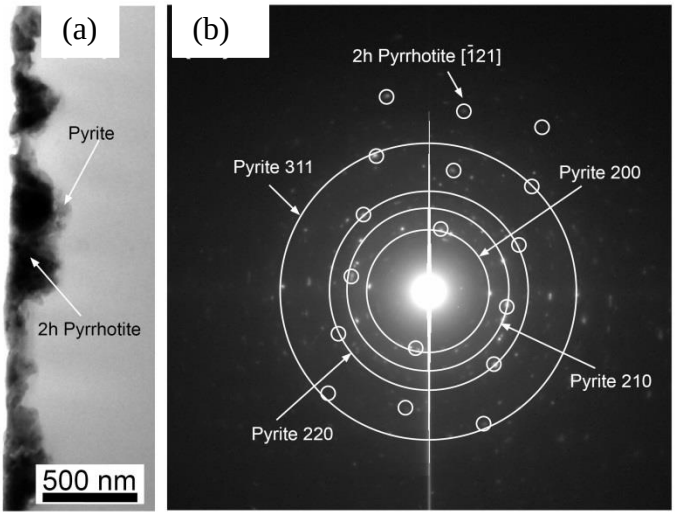

Fig. 24. a) TEM image of the sample of pyrite thin film grown at a substrate temperature of 350 °C, a S pressure of 1 Torr, and cooled in a 1 Torr S pressure, showing a layer of pyrite adjacent to a 125-nm thick layer of pyrrhotite, c) TEM diffraction pattern showing pyrrhotite diffraction spots and pyrite rings. The film described here was synthesized at a growth rate of 0.2 monolayers per second.

Ex-situ S-annealing experiments were performed on > 100 nm, $Fe_{1-x}S$ and Fe-metal films to investigate temperature and S pressure required to convert them to pyrite (FeS_2). Table. 3 summarizes the conditions that were used. The lowest S pressure possible to obtain in the sealed tubes was ~50 Torr.

Table. 3. Fe and $Fe_{1-x}S$ films annealing condition in S

Film type	**T_a (°C)**	**P_s (Torr)**
FeS_x (x<2)	350	50
Fe and FeS_x (x<2)	350	500
Fe and FeS_x (x<2)	500	50
Fe and FeS_x (x<2)	500	500

XRD results of the samples after annealing, Fig. 25, showed both Fe-metal and $Fe_{1-x}S$ films were converted to polycrystalline pyrite indicating that either the $Fe_{1-x}S$ or the Fe films can be converted to pyrite at these temperatures under sufficient S pressure, as predicted by the phase diagram of Waldner and Pelton [60].

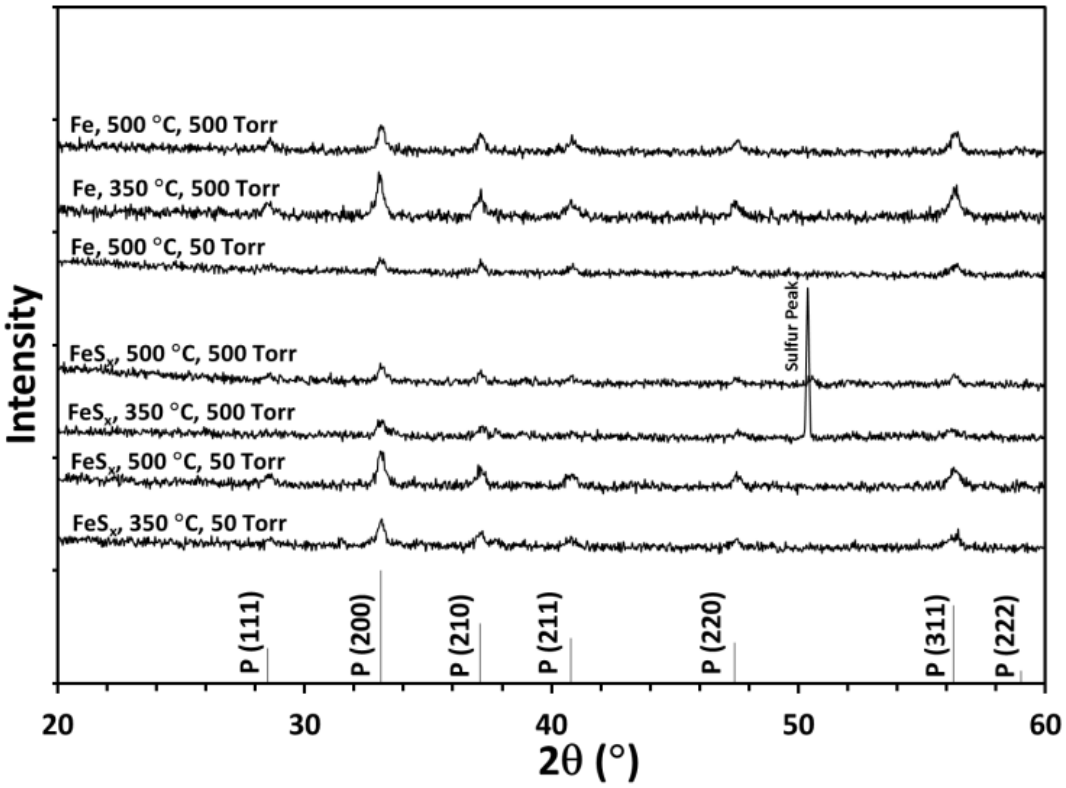

Fig. 25. XRD analysis of ex-situ annealing experiment in sulfur on Fe and $Fe_{1-x}S$ thin films grown on SiO_x/Si substrate and sealed in glass tube.

The results of co-evaporation and ex-situ annealing in S can be summarized as follows:

- In vacuum above 100 °C films are S deficient ($Fe_{1-x}S$), even at P_S as high as 1 Torr
- Upon cooling in 1 Torr P_S at temperature <350 °C, $Fe_{1-x}S$ converts to pyrite
- Upon annealing ex-situ in P_S > 50 Torr, both Fe-metal or $Fe_{1-x}S$ converts to pyrite at 500 °C temperatures

To overcome the kinetic barrier of forming FeS_2, I devised a layer-by-layer growth method, to operate at elevated temperatures (i.e., 350-500 °C), that consists of sequential evaporation of Fe in vacuum followed by exposure to a high-pressure (i.e., up to 1 Torr) S environment. The reduced pressure of S during deposition of Fe and absence of Fe during incorporation of S enhances adatom surface mobility during each step, which increases the driving force for each reaction. This sequential evaporation method enabled growth of single-phase pyrite with vastly improved quality than with the traditional MBE method (Fig. 26 and 27). However, both of the films are polycrystalline. The sequential-evaporation film was grown at 350 °C by applying only 1 mTorr S pressure to the sulfidation zone. RBS results confirmed that the film grown by sequential method has a 240-nm thickness and a stoichiometry of $FeS_{2.04}$.

Fig. 26 shows the XRD spectra of the film grown by this sequential method compared to the best film grown by the co-evaporation method. Fig. 27-a, and b shows the SEM comparison of the pyrite films at 350 °C grown by sequential evaporation and

co-evaporation method. The SEM images indicate the films grown with the sequential-evaporation method are smoother than the films prepared by co-evaporation.

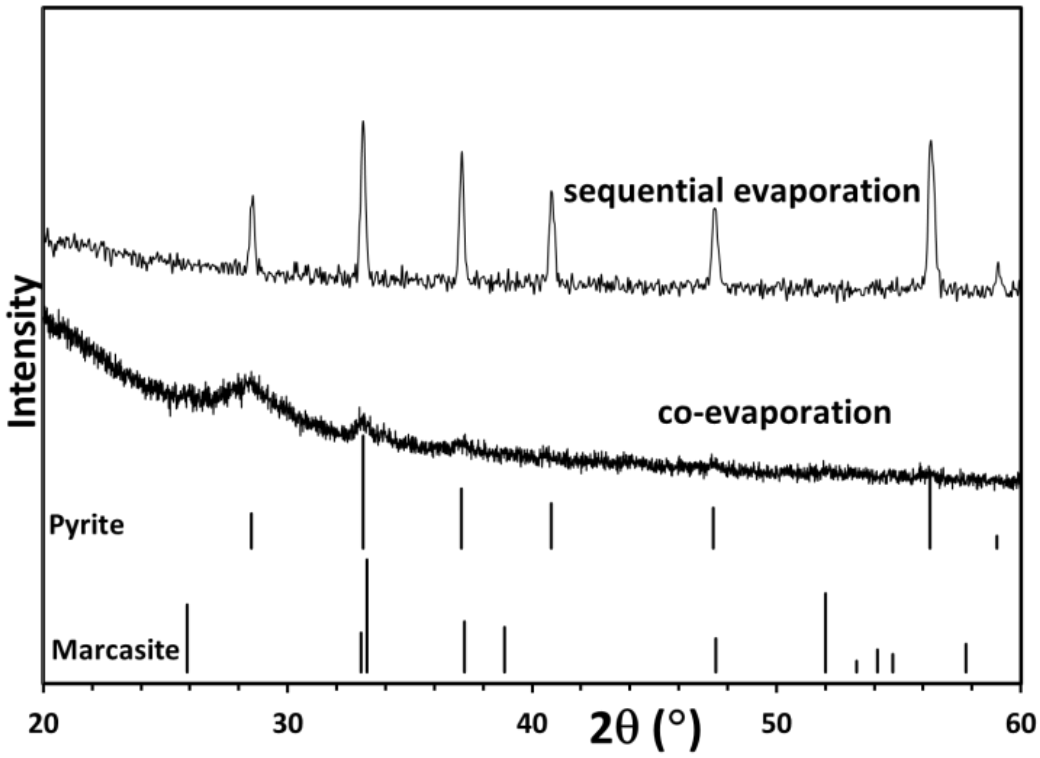

Fig. 26. Comparison of XRD spectra for a thin-film grown by sequential evaporation at a substrate temperature of 350 °C and S pressure of 1 mTorr (upper) with MBE films grown and cooled at a S pressure of 1 Torr and substrate temperature of 350 °C (lower). The sequentially evaporated $FeS_{2.04}$, film was 240-nm thick, indicating a growth rate of ~1 monolayer per cycle.

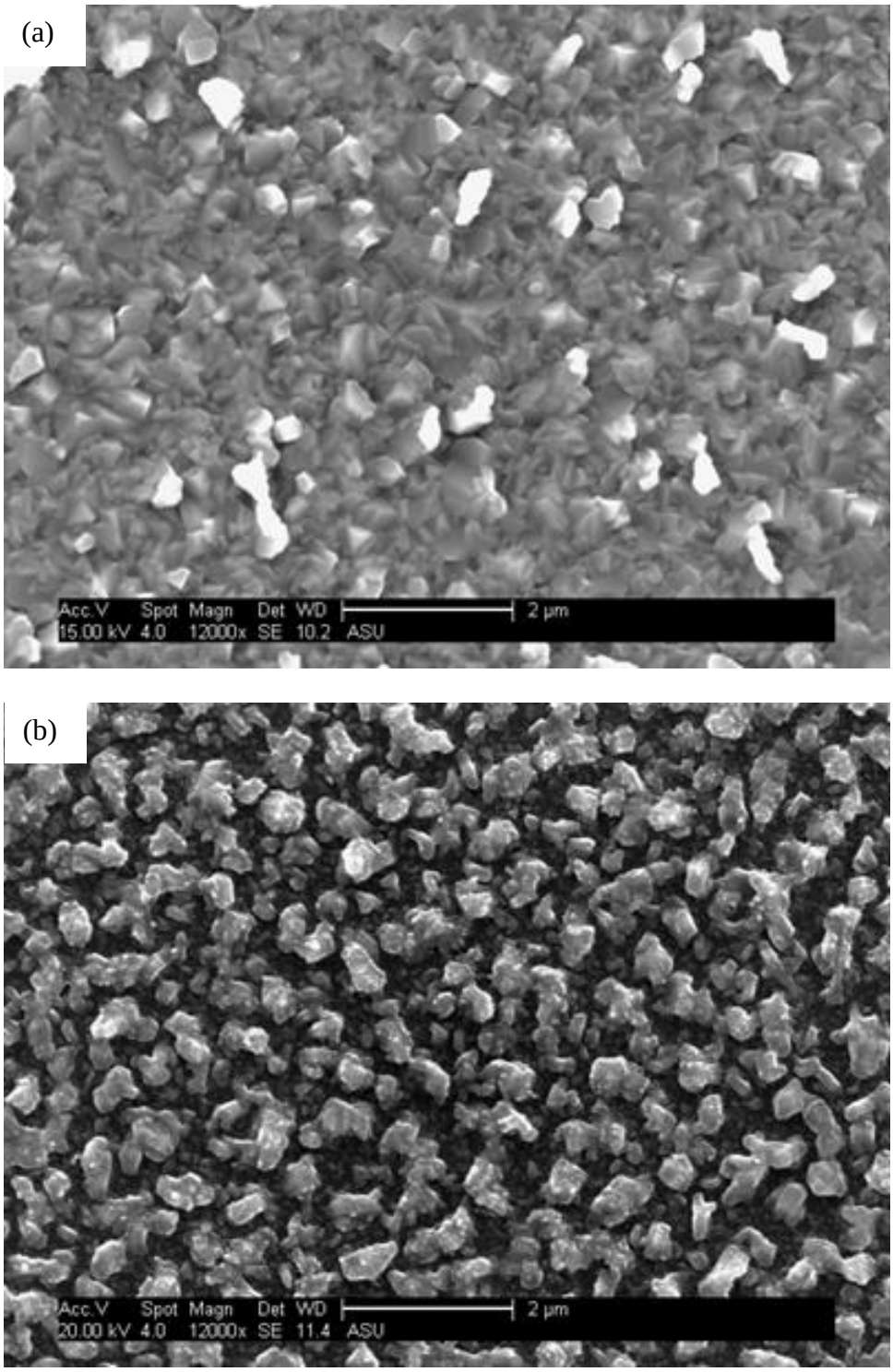

Fig. 27. SEM images of the films deposited at 350 °C by, a) sequential evaporation at 1 mTorr S pressure, and b) co-evaporation at 1 mTorr S pressure.

The effect of substrate temperature on the quality of pyrite thin films prepared by sequential evaporation was systematically investigated. For the substrate temperatures ranging from 250 to 450 °C, pyrite films were polycrystalline. The structural quality, as judged by the narrowest XRD peaks at full-width half-maximum, increased with substrate temperature and was optimized at 350 °C for a S pressure of 1 mTorr (Fig. 28-a). Secondary phases were not detected by XRD and Raman spectroscopy for films grown at substrate temperatures up to 375 °C. However, marcasite (tetragonal FeS_2) was detected using both XRD and Raman in films grown above 375 °C. SEM images of pyrite films deposited at different substrate temperatures by sequential evaporation (Fig. 29) indicate that the films tend to grow more granular at higher temperatures. At 450 °C the pyrite films are discontinuous, as confirmed by the substrate peak (Si peak) in the Raman results (Fig. 28-b), and have tower shaped morphology.

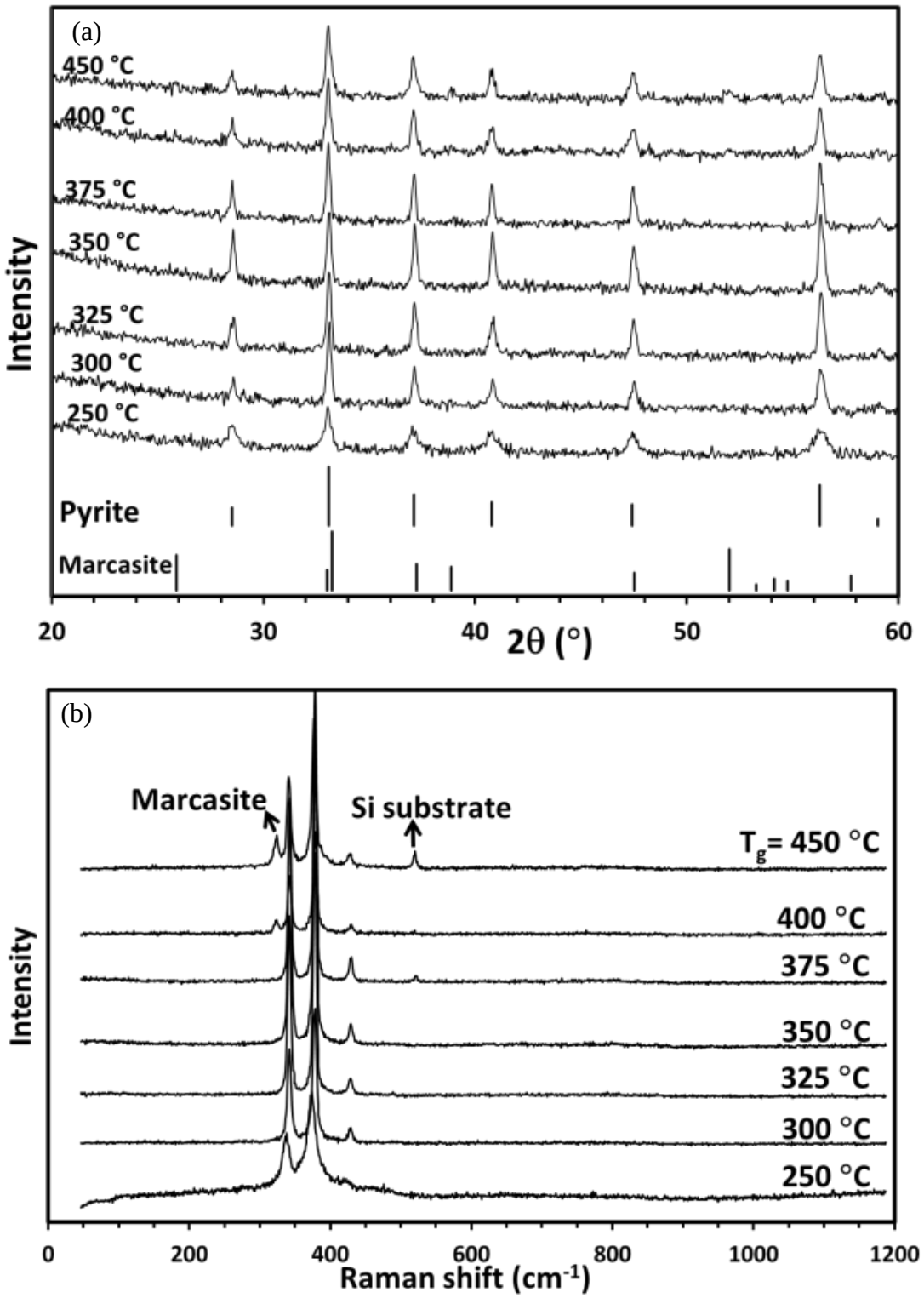

Fig. 28. a) XRD and b) Raman spectra of sequentially deposited pyrite films grown on Si (100) at different substrate temperatures and a S pressure of 1 mTorr with a growth rate of 1 to 2 monolayers per cycle .

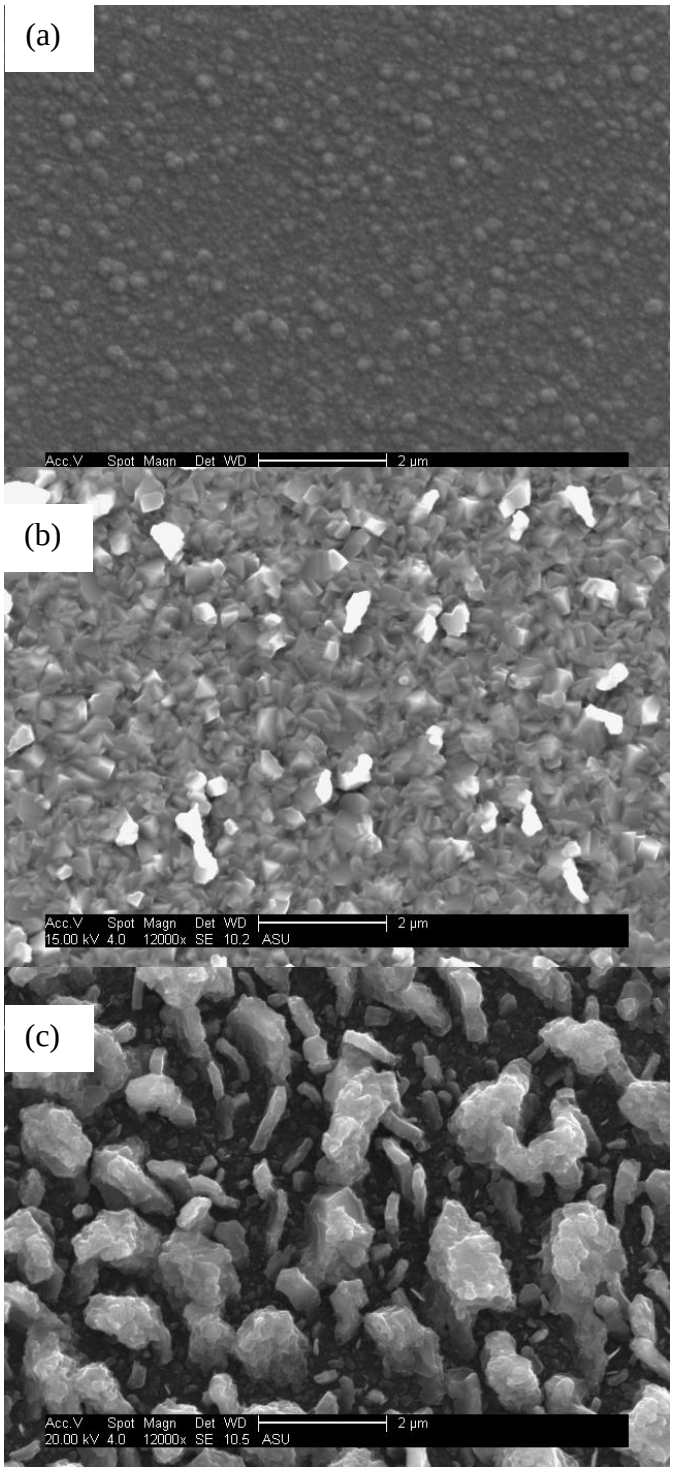

Fig. 29. SEM image of pyrite thin films grown by sequential evaporation on Si substrate at S pressure of 1 mTorr and substrate temperature of, a) 250 , b) 350, and c) 450 °C.

Films deposited on SiO_x/Si, Al_2O_3, and MgO substrates have similar structural and chemical properties, as judged by XRD, Raman and RBS analysis. Fig. 30, shows the presence of a marcasite peak in Raman data for films grown at 400 °C and a S pressure of 1 mTorr on Si (111) and Al_2O_3.

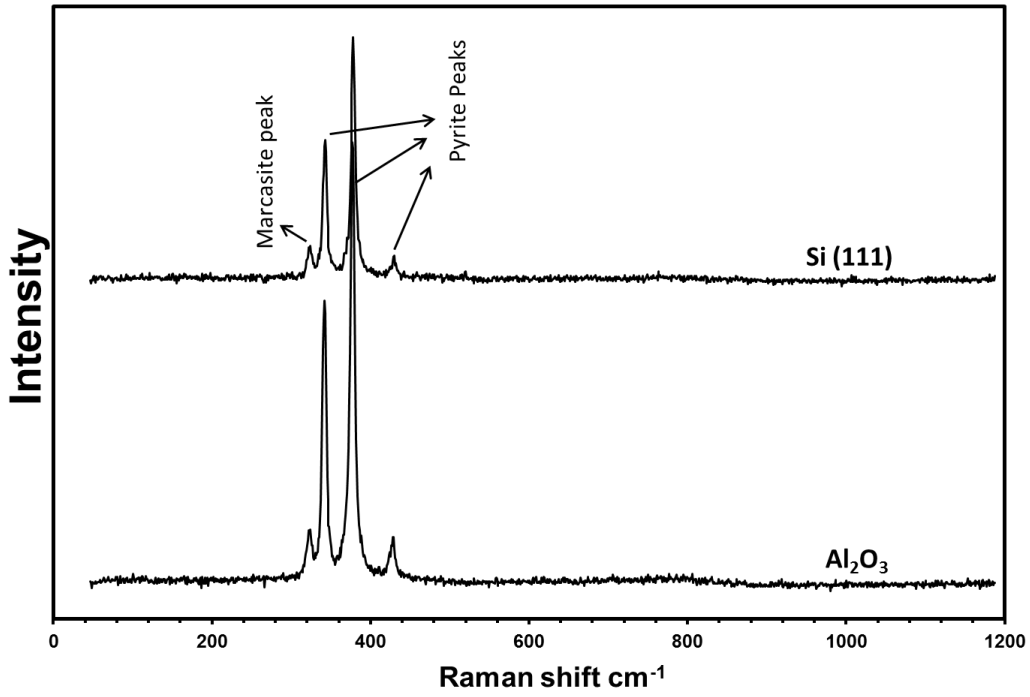

Fig. 30. Effect of substrate type on pyrite growth, substrate temperature 400 °C.

Increasing the S pressure to 1 Torr resulted in the formation of single-phase pyrite films at substrate temperatures up to 450 °C (Fig. 31). The use of high-S pressures during growth and cool-down in the MOCVD study of Thomas et al. [7] also produced stoichiometric pyrite at 450 - 500 °C. Both these results are consistent with the Fe-S phase diagram [60], which indicates that pyrite is stable up to 550 °C at S pressure of 1 Torr.

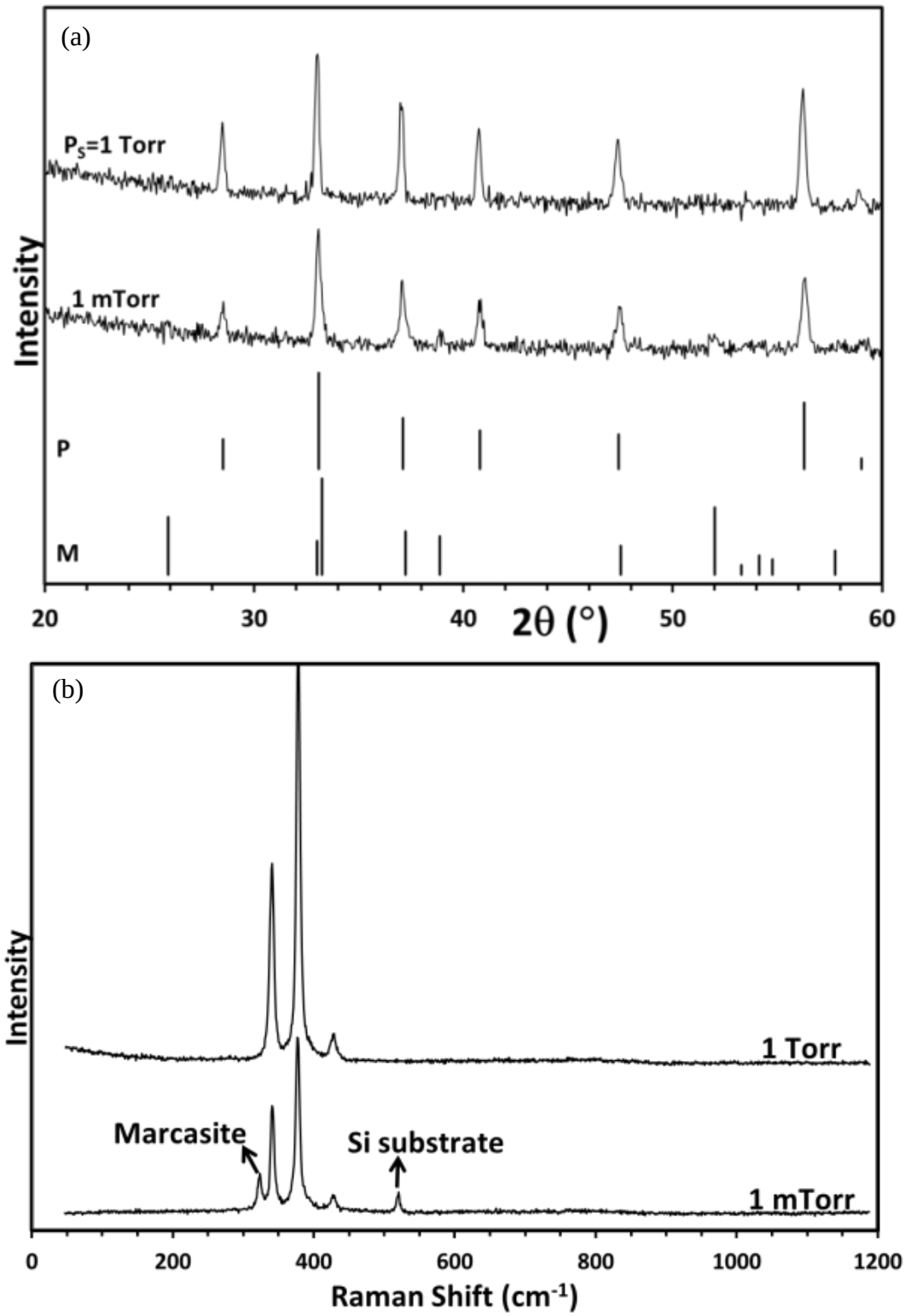

Fig. 31. a) XRD and b) Raman spectra of pyrite films produced using sequential evaporation at 450 °C substrate temperatures at a S pressure of 1 mTorr (lower) and 1 Torr (upper).

Pyrite films grown on Si (100) substrates at 350 °C and S pressures of 1mTorr consist of randomly oriented grains ~300 to 400 nm in diameter (Fig. 32-a, b). Since the lattice mismatch of pyrite and Si is less than 2%, it should be possible to deposit epitaxial pyrite on Si. However, high-resolution TEM images indicate that the high-quality, defect-free grains are separated from the substrate by a ~3 nm amorphous SiO_x layer (Fig. 32-c). This amorphous layer presumably resulted in non-epitaxial polycrystalline growth of pyrite on the Si substrate. Therefore, improved substrate cleaning methods are needed to achieve epitaxy on Si substrates. Fig. 32 also, shows STEM annular dark field and annular bright-field images of the pyrite grain indicating the positions of the atoms in the structure. The crystallographic model of the projection of the pyrite structure, with the Fe and the S atoms is shown in the inset of Fig 32-e. The S dumbbells can be clearly identified in this image. This observation is in agreement with the proposed structure of pyrite [61, 62] and represented in Fig. 33.

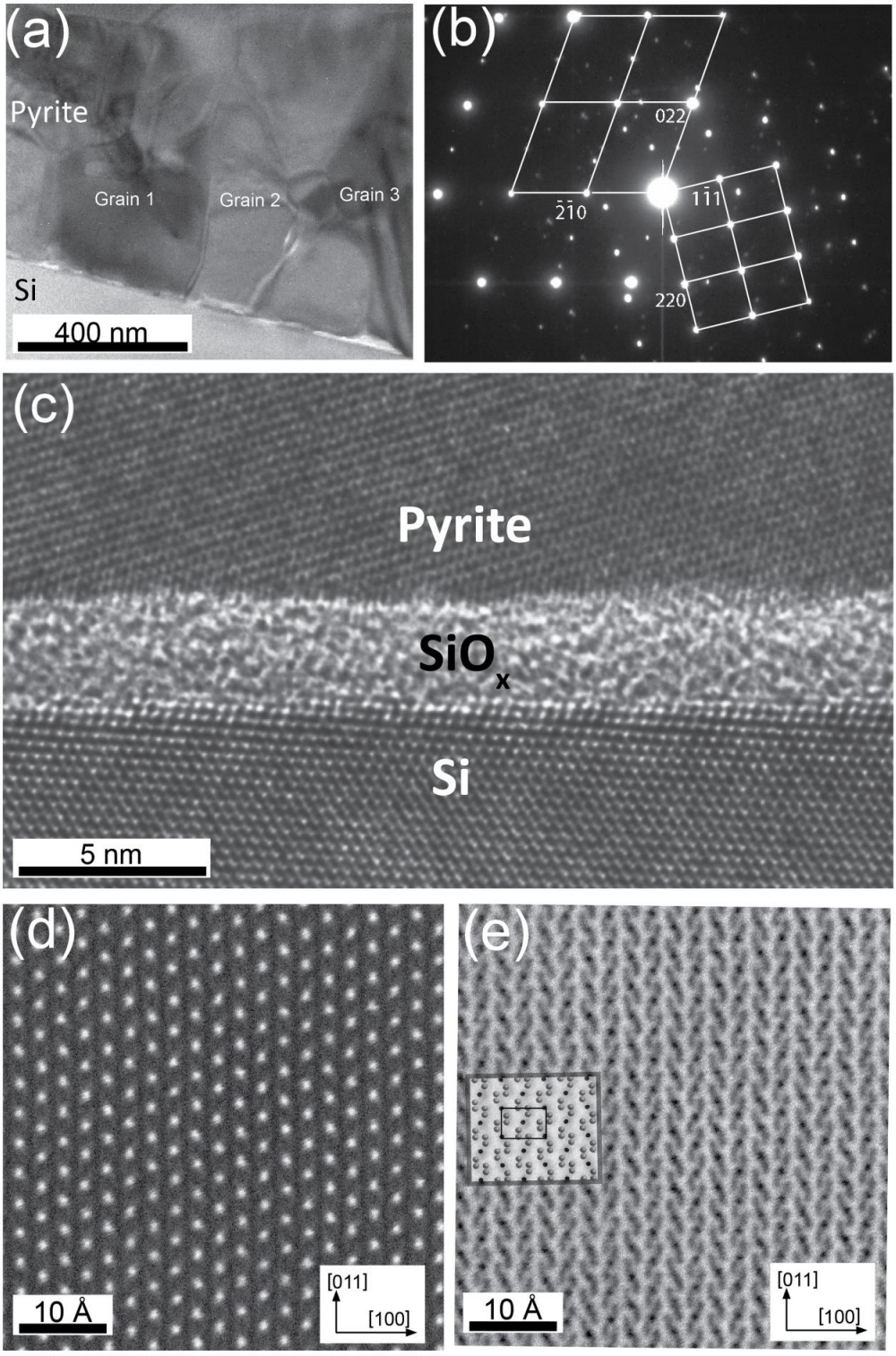

Fig. 32. a) TEM image of 400-nm pyrite grains grown on Si (100) substrate at 350 °C and a S pressure of 1 mTorr, b) diffraction pattern indexed for two pyrite grains, c) HRTEM image of pyrite grain (top) at the interface with Si substrate (bottom). The SiO_x layer

formed by oxidation of Si substrate, d) STEM annular dark-field image of defect-free pyrite grain from a); the bright spots are the Fe columns. e) STEM annular bright-field image of the same grain showing the positions of the S atoms. The inset is a crystallographic model of the projection of the pyrite structure, with the Fe atoms represented by black dots and the S atoms represented by the grey spheres. The black rectangle outlines a unit cell.

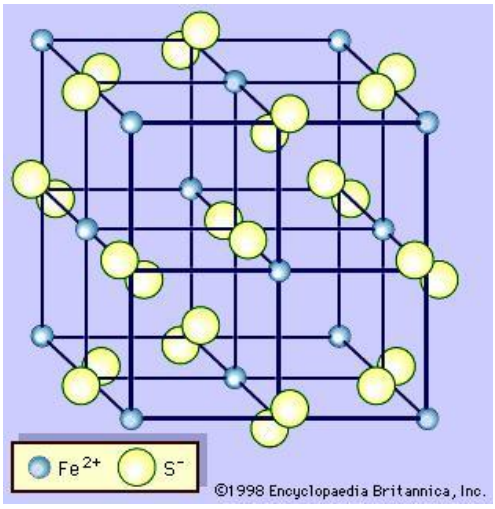

Fig. 33. Pyrite structure, showing the Fe and S dumbbells [62].

Non-epitaxial polycrystalline pyrite films have been grown using a number of methods on a wide range of substrates, even on those with small lattice mismatch (e.g., ZnS, Si, and GaP) [52-57, 63-66]. To produce epitaxial structures, the use of the sequential evaporation method was investigated by deposition on natural pyrite substrates. For this homo-epitaxy study, I started with two ~1-cm^2 (100) oriented faces from natural pyrite cubes. Growth was performed at a 350 °C substrate temperature and S pressure of 1 mTorr. Si substrates were included as a control.

Channeling RBS measurements were used to characterize the epitaxial quality of thin films. Channeling RBS χ_{min} of 3% was determined for the natural pyrite substrate (Fig. 34-a), and a χ_{min} of 11% for the deposited thin-film on natural pyrite (Fig. 34-b).

When compared to the ~58% χ_{min} for the film grown on Si (111) (Fig. 34-c), it is clear that the film grown on natural pyrite exhibits textured (epitaxial) characteristics. The XRD results of the pyrite films on natural pyrite (Fig. 35) show that the films has a preferred growth orientation compared to the film grown on Si substrate.

High-resolution TEM images of pyrite films grown on natural pyrite substrates indicate (Figs. 36 and 37) that the films consist of individual grains that are 100 to 150 nm diameter and grown epitaxially. The presence of individual epitaxial grains indicates heterogeneous nucleation on natural pyrite. In addition, many of the grains have stacking faults.

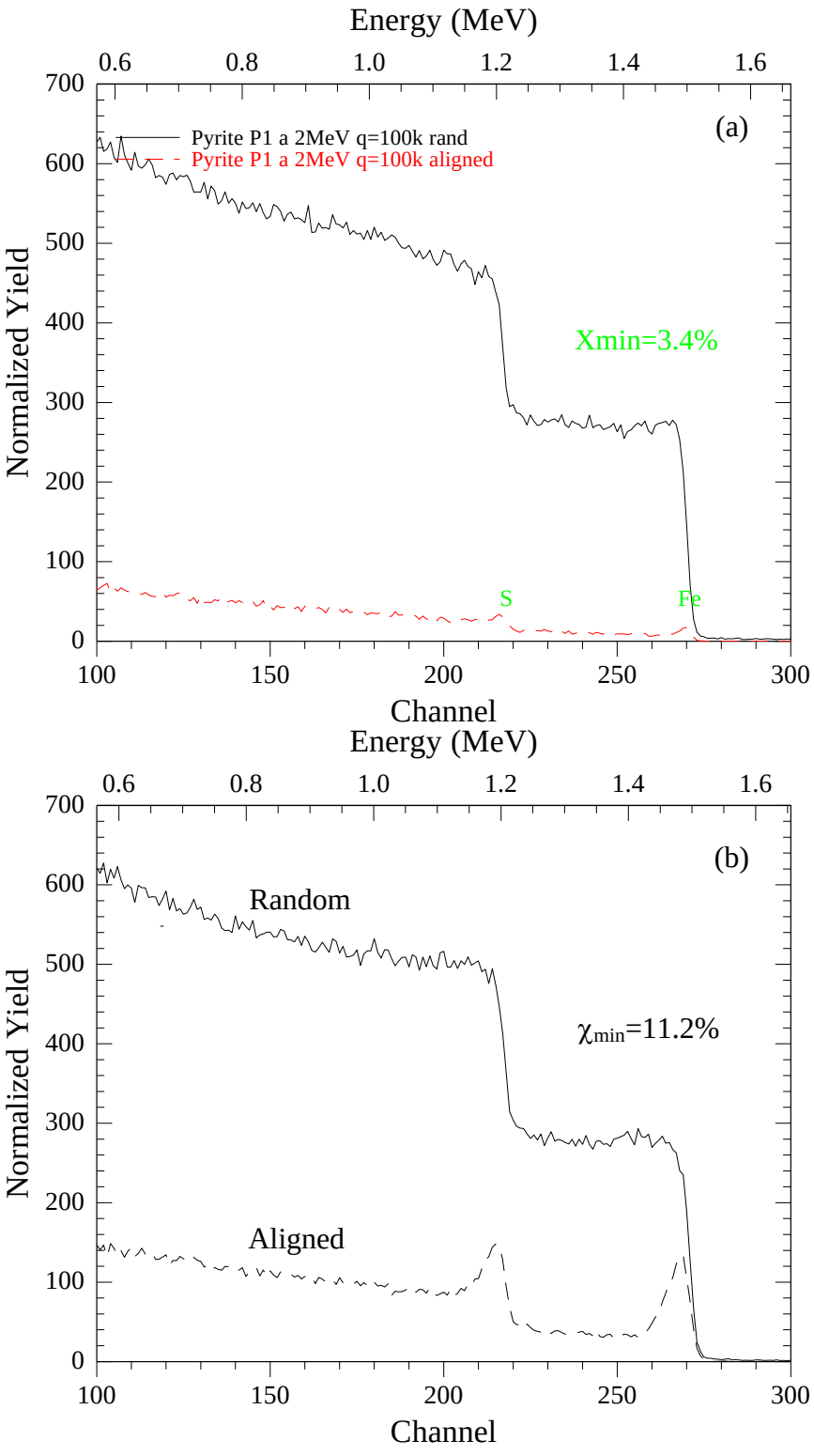
Energy (MeV)
0.6
0.8
1.0
1.2
1.4
1.6
Normalized Yield
Channel
Pyrite P1 a 2MeV q=100k rand
Pyrite P1 a 2MeV q=100k aligned
(a)
Xmin=3.4%
S
Fe
(b)
Random
Aligned
χmin=11.2%

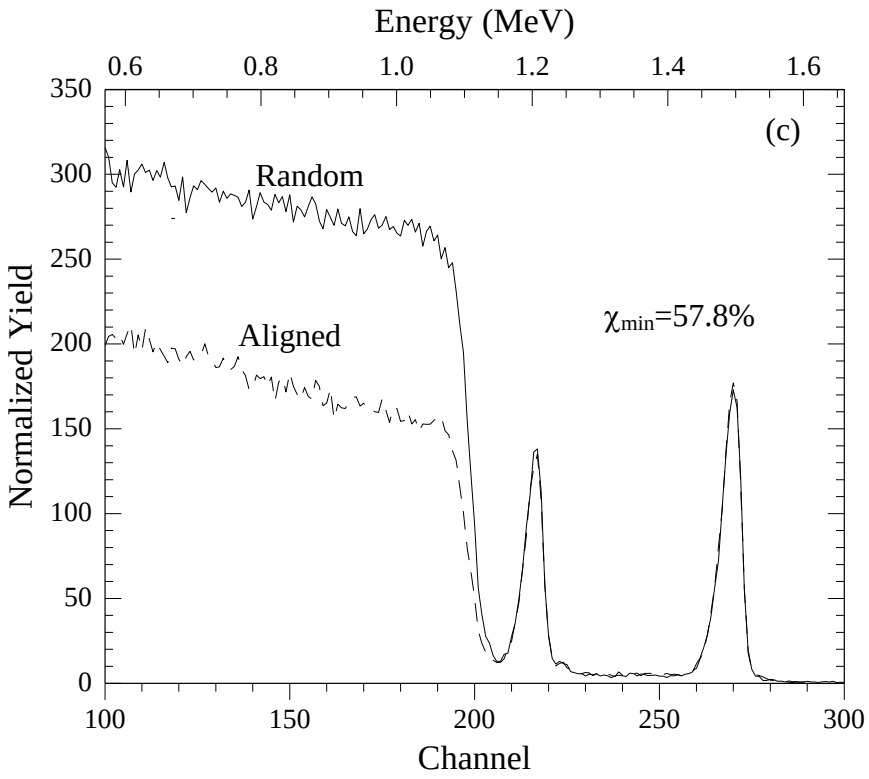

Fig. 34. RBS channeling results from a) natural pyrite (100) substrate; pyrite films grown at 350 °C and a S pressure of 1 mTorr on: b) natural pyrite showing homo-epitaxy, and c) a Si substrate.

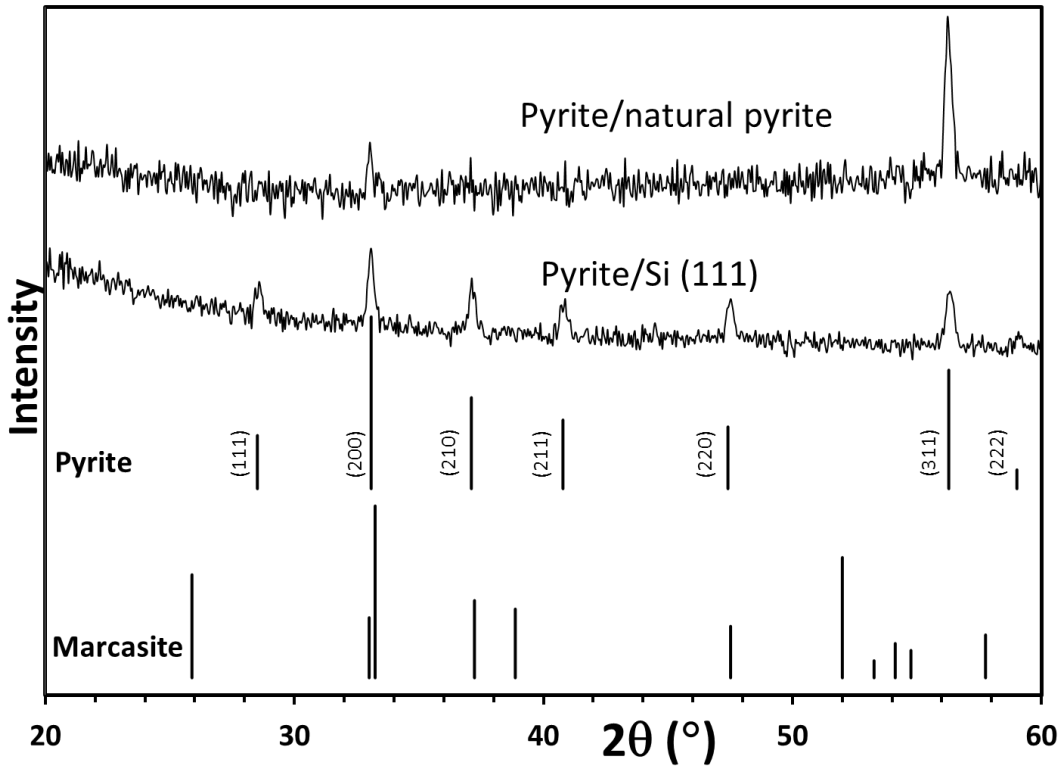

Fig. 35. XRD comparison of pyrite thin film deposited at 350 °C and a S pressure of 1 mTorr on natural pyrite (100) (upper), and Si (lower) substrates.

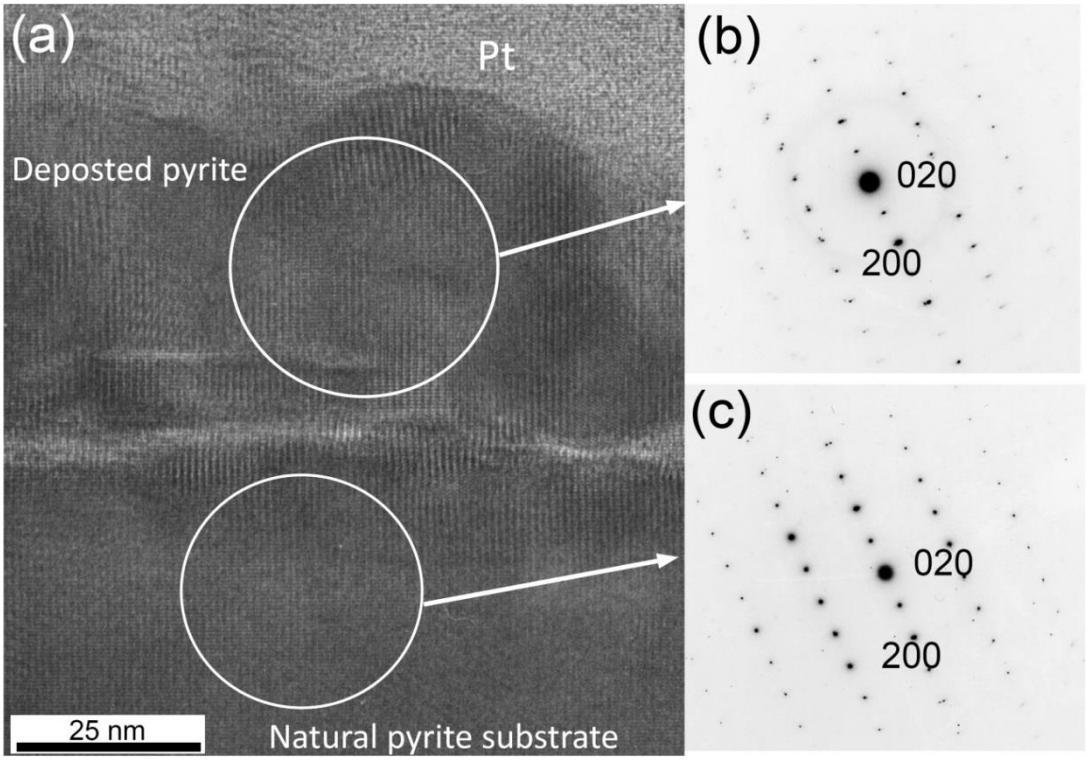

Fig. 36. a) TEM image of a homo-epitaxial pyrite thin film grown on natural pyrite at 350 °C and 1 mTorr S pressure , b) and c) diffraction patterns from the thin film and substrate respectively.

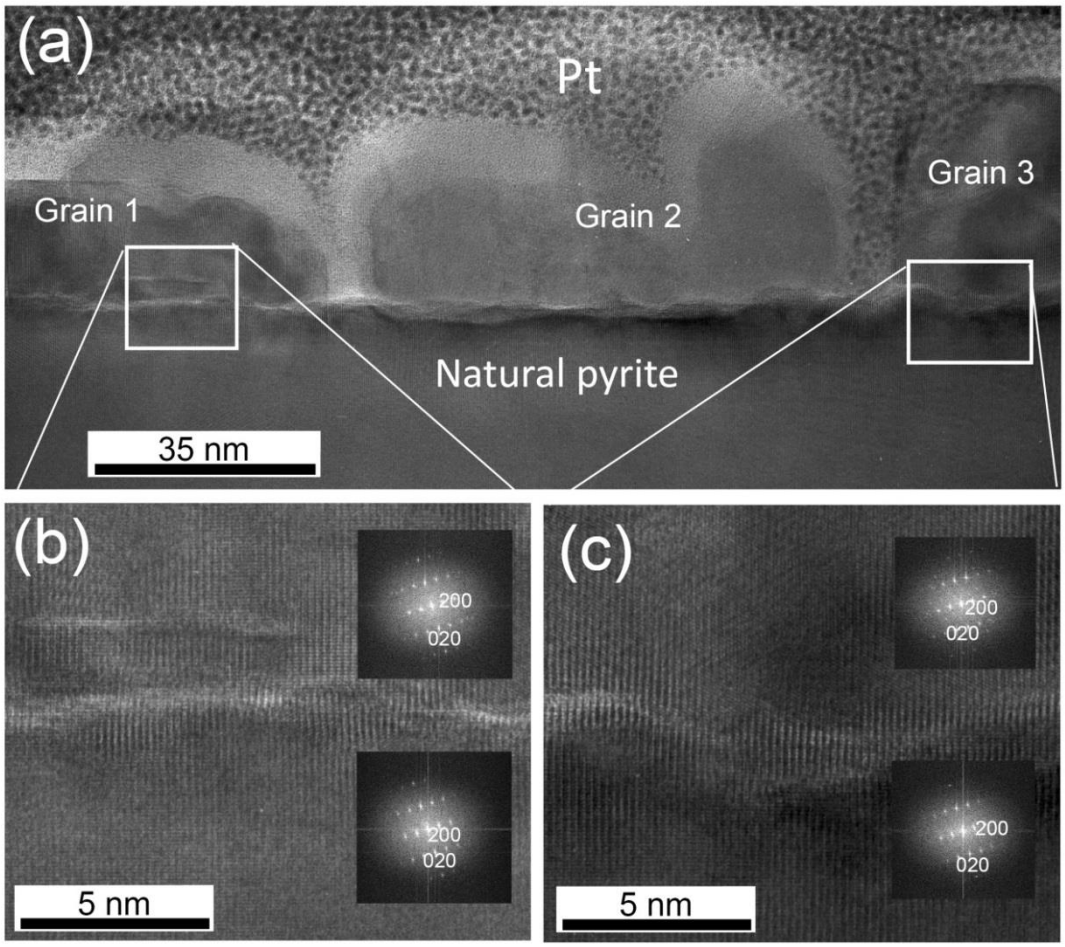

Fig. 37. a) HRTEM images of individual homo-epitaxial grains from a pyrite thin film grown at 350 °C and S pressure of 1 mTorr, b) and c) close up images of the grains indicating epitaxial growth. Insets are Fast Fourier Transforms of the grains(top) and substrate (bottom).

Current-Voltage (I-V) electrical measurements in a 2-point configuration were performed on the pyrite film grown on an insulator substrate (SiO_x/Si) at 300 °C and a S pressure of 1 mTorr. A photo response of ~5% was detected in the film, Fig. 38. The resistivity of this sample was measured from 20-300 K using four point measurement and Van der Pauw configuration (Fig. 39). The data follow a liner fit of resistivity versus $T^{-0.5}$, indicating that the dominant transport mechanism is variable-range hopping [67, 68].

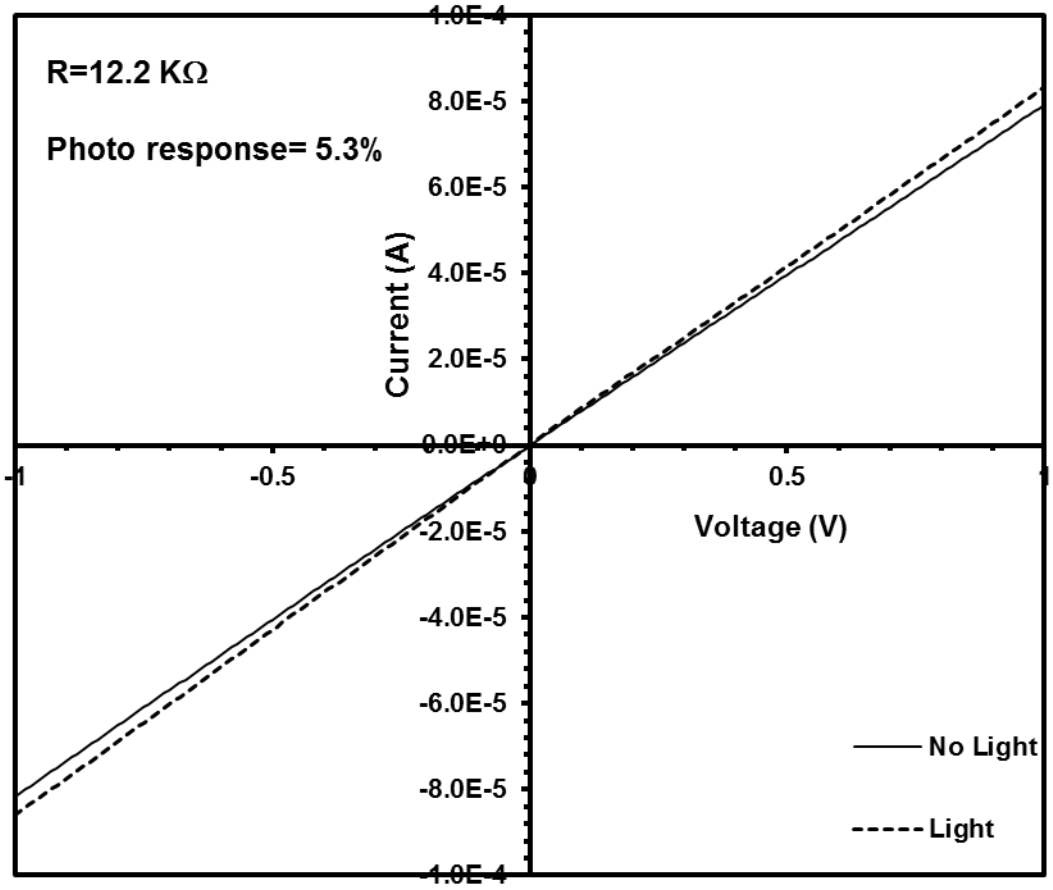

Fig. 38, Photo response of pyrite film deposited at 300 °C and a S pressure of 1 mTorr measured by I-V using two point probe measurement.

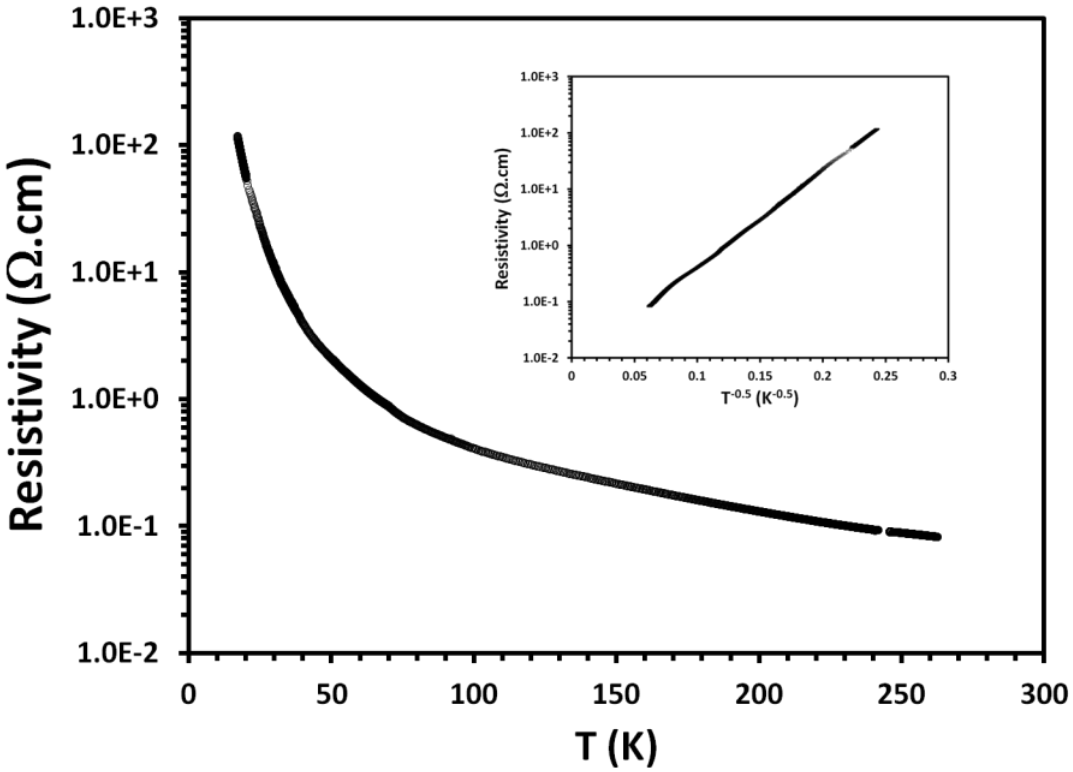

Fig. 39. Resistivity vs. temperature for sample grown on SiO_x/Si at 300 °C and a S pressure of 1 mTorr; inset: data fitted to the hopping model. The error in the current measurement is less than 2%.

4.4. Conclusions

Based on the thermochemical analysis and experimentation with pyrite thin film growth, it was concluded that a layer-by-layer growth method is needed to overcome the kinetic barrier to deposition of single phase pyrite films. A new deposition technique was developed and it is demonstrated that high quality, single phase pyrite can be grown with this new technique. An epitaxial pyrite thin film was successfully deposited on natural pyrite. A photo response more than 5% was detected in pyrite films. Results of the resistivity measurements indicated that variable range hopping is the dominant carrier transport mechanism in the deposited pyrite thin films.

Chapter 5

CONCLUSIONS

In conclusion, it is demonstrated that CFAS electrodes with a native Al oxide barrier can be used as an injector of spin-polarized electron populations. The growth, structure, magnetic characterization, and spin polarization of CFAS thin films were systematically studied. A highly ordered $L2_1$ structure of CFAS films was achieved by growing in a 1-step process at substrate temperatures of more than 350 °C. Sputtered CFAS thin films prepared with both the 1-step and 2-step process exhibited excellent magnetic properties. Using the PCAR method, high spin polarization at the surface of the CFAS thin films of over 70%, was detected. The use of an AlO_x oxide barrier in superconducting/insulator/CFAS structures resulted in mostly direct tunneling, while structures with CFAS native oxide barriers did not.

The $ZnGeAs_2$ PLD growth and thermal decomposition studies showed that the substrate temperature needed to achieve high-quality $ZnGeAs_2$ epitaxy is not limited by the low sticking coefficients of Zn and As alone but is, in fact, largely determined by the kinetic barrier to decomposition. Due to this large kinetic barrier to decomposition, with an evaporation coefficient of 10^{-4}-10^{-2}, high quality films can be grown in the metastable regime.

High-quality pyrite (FeS_2) thin films can be synthesized using a layer-by-layer growth technique with sequential evaporation of Fe in high-vacuum followed by sulfidation at pressures between 1 mTorr and 1 Torr at temperatures between 250 and 450 °C. Additionally, pyrite can be grown epitaxially on natural pyrite substrates. Electrical

measurements indicate that the dominant transport in the films produced is by variable-range hopping and a photo response more than 5% was detected in pyrite films

REFERENCES

1. I. Galanakis and P. H. Dederichs, “Half-Metallic Alloys”, Lect. Notes Phys., Springer, Berlin Heidelberg, 2005, 4.

2. N. Tezuka, N. Ikeda, F. Mitsuhashi, S. Sugimoto, “Improved tunnel magnetoresistance of magnetic tunnel junctions with Heusler $Co_2FeAl_{0.5}Si_{0.5}$ electrodes fabricated by molecular beam epitaxy”, Appl. Phys. Lett., 94 (2009) 162504.

3. D. J. Monsma and S. S. P. Parkin, “Spin polarization of tunneling current from ferromagnet/Al_2O_3 interfaces using copper-doped aluminum superconducting films”, Appl. Phys. Lett., Vol. 77, 5 (2000) 31.

4. R. Shan, H. Sukegawa, W. H. Wang, M. Kodzuka, T. Furubayashi, T. Ohkubo, S. Mitani, K. Inomata, K. Hono, “Demonstration of Half-Metallicity in Fermi-Level-Tuned Heusler Alloy $Co_2FeAl_{0.5}Si_{0.5}$ at Room Temperature”, Phys. Rev. Lett., 102 (2009) 246601.

5. W. Wang, H. Sukegawa, R. Shan, T. Furubayashi, K. Inomata, “Preparation and characterization of highly $L2_1$-ordered full-Heusler alloy $Co_2FeAl_{0.5}Si_{0.5}$ thin films for spintronics device applications”, Appl. Phys. Lett., 92 (2008) 221912.

6. W. Wang, H. Sukegawa, R. Shan, and K. Inomata, “Large tunnel magnetoresistance in $Co_2FeAl_{0.5}Si_{0.5}$/MgO/ $Co_2FeAl_{0.5}Si_{0.5}$ magnetic tunnel junctions prepared on thermally oxidized Si substrates with MgO buffer”, Appl. Phys. Lett., 93 (2008) 182504.

7. S. W. Lehner, N. Newman, M. van Schilfgaarde, S. Bandyopadhyay, K. Savage, P. R. Buseck, “Defect energy levels and electronic behavior of Ni-, Co-, and As-doped synthetic pyrite (FeS_2)”, J. Appl. Phys., 111 (2012) 083717.

8. T. J. Peshek, L. Zhang, R. K. Singh, Z. Tang, M. Vahidi, B. To, T. J. Coutts, T. A. Gessert, N. Newman, M. van Schilfgaarde, “Criteria for improving the properties of $ZnGeAs_2$ solar cells”, Prog. Photovolt: Res. Appl., (2012).

9. S. I. Shah and J. E. Greene, “Growth and physical properties of amorphous and single crystal $ZnGeAs_2$ layers deposition on (100) GaAs by sputter deposition in excess Zn and As_4”, J. Cryst. Growth, 68 (1984) 537.

10. B. Chelluri, T. Y. Chang, A. Ourmazd and A. H. Dayem, “Molecular beam epitaxial growth of II-V semiconductor $Zn3As_2$ and II-IV-V chalcopirite $ZnGeAs_2$”, J. Cryst. Growth, 81 (1987) 530.

11. G. S. Solomon, M. L. Timmons, J. B. Posthill, “Antiphase domain boundary formation in single-crystal chalcopyrite structure $ZnGeAS_2$ grown on GaAs”, J.

Appl. Phys., 65 (1989) 1952.

12. M. L. Timmons and K. J. Bachmann, "Growth of NLO chalcopyrite materials by OMVPE", Mat. Res. Soc. Symp. Proc., 484 (1998) 507.

13. C. HÖpfner, K. Ellmer, A. Ennaoui, C. Pettenkofer, S. Fiechter, H. Tributsch, "Stoichiometry-, phase- and orientation-controlled growth of polycrystalline pyrite (FeS_2) thin films by MOCVD", J. Cryst. Growth, 151 (1995) 325.

14. B. Thomas, T. Cibik, C. HÖpfner, K. Diesner, G. Ehlers, S. Fiechter, K. Ellmer, "Formation of secondary iron-sulfur phase during the growth of polycrystalline iron pyrite (FeS_2) thin films by MOVCD", J. Mater. Sci. Mater. El., 9 (1998) 61.

15. H. Sukegawa, W. Wang, R. Shan, T. Nakatani, K. Inomata, K. Hono, "Spin-polarized tunneling spectroscopy of fully epitaxial magnetic tunnel junctions using $Co_2FeAl_{0.5}Si_{0.5}$ Heusler alloy electrodes", Phys. Rev. B, 79 (2009)184418.

16. http://en.wikipedia.org/wiki/Tunnel_magnetoresistance

17. http://physicsworld.com/cws/article/print/2008/jan/03/the-spintronics-challenge

18. Z. Gercsi, A. Rajanikanth, Y. K. Takahashi, K. Hono, M. Kikuchi, N. Tezuka, K. Inomata, "Spin polarization of Co_2FeSi full-Heusler alloy and tunneling magnetoresistance of its magnetic tunneling junctions", Appl. Phys. Lett., 89 (2006) 082512.

19. R. J. Soulen, M. S. Osofsky, B. Nadgorny, T. Ambrose, P. Broussard, S. F. Cheng, J. Byers, C. T. Tanaka, J. Nowack, J. S. Moodera, G. Laprade, A. Barry, M. D. Coey, "Andreev reflection: A new means to determine the spin polarization of ferromagnetic materials", J. Appl. Phys., Vol. 85, 8 (1999) 4589.

20. T. Y. Chen, S. X. Huang, and C. L. Chien, "Pronounced effects of additional resistance in Andreev reflection spectroscopy", Phys. Rev. B, 81 (2010) 214444.

21. T. Y. Chen, Z. Tesanovic, and C. L. Chien, "Unified Formalism of Andreev Reflection at a Ferromagnet/Superconductor Interface", Phys. Rev. Lett., 109 (2012) 146602.

22. S. Trudel, G. Wolf, J. Hamrle, B. Hillebrands, P. Klaer, M. Kallmayer, H. J. Elmers, H. Sukegawa, W. Wang, K. Inomata, "Effect of annealing on $Co_2FeAl_{0.5}Si_{0.5}$ thin films: A magneto-optical and x-ray absorption study", Phys. Rev. Lett., 83 (2011) 104412.

23. P. J. Webster, "Magnetic and chemical order in Heusler alloys containing cobalt and manganese", J. Phys. Chem. Solids, 32 (1971) 1221.

24. S. Wurmehl, G. H. Fecher, H. C. Kandpal, V. Ksenofontov, and C. Felser,

"Geometric, electronic, and magnetic structure of Co_2FeSi: Curie temperature and magnetic moment measurements and calculations", Phys. Rev. B, 72 (2005) 184434.

25. N. Tezuka, N. Ikeda, A. Miyazaki, S. Sugimoto, M. Kikuchi, and K. Inomata, "Tunnel magnetoresistance for junctions with epitaxial full-Heusler $Co_2FeAl_{0.5}Si_{0.5}$ electrodes with B2 and $L2_1$ structures", Appl. Phys. Lett., 89 (2006) 112514.

26. T. M. Nakatani, A. Rajanikanth, Z. Gercsi, Y. K. Takahashi, K. Inomata, and K. Hono, "Structure, magnetic property, and spin polarization of $Co_2FeAl_xSi_{1-x}$ Heusler alloys", J. Appl. Phys., 102 (2007) 033916.

27. G. Schmidt, D. Ferrand, L.W. Molenkamp, A.T. Filip, and B.J. van Wees, "Fundamental obstacle for electrical spin injection from a ferromagnetic metal into a diffusive semiconductor", Phys. Rev. B, 62 (2000) R4790.

28. E. I. Rashba, "Theory of electrical spin injection: Tunnel contacts as a solution of the conductivity mismatch problem", Phys. Rev. B, 62 (2000) R16267.

29. N. Tombros et al., "Electronic spin transport and spin precession in single graphene layers at room temperature", Nature, 4482 (2007) 571.

30. L.Y. L. Shen and J. M. Rowell, "Zero-Bias Tunneling Anomalies-Temperature, Voltage, and Magnetic Field Dependence", Phys. Rev., 165 (1968) 566.

31. H. R. Zeller and I. Giaever, "Tunneling, Zero-Bias Anomalies, and Small Superconductors", Phys. Rev., Vol. 181, 2 (1969) 180.

32. J. Y. Tsao, "Materials Fundamentals of Molecular Beam Epitaxy", Academic Press Inc, San Diego, 1993.

33. J. L. Vossen, W. Kern, Thin-Film Processes II, Academic Press Inc, New York, 1991.

34. F. W. Scholl and E. S. Cory., "Preparation and properties of $ZnGeAs_2$", Materials Research Bulletin, 9 (1974) 1511.

35. P. Hohenberg and W. Kohn, "Inhomogeneous electron gas", Phys. Rev. B, 864 (1964) 136.

36. J. P. Perdew, K. Burke, M. Ernzerhof, "Generalized Gradient Approximation Made Simple", Phys. Rev. Lett., 77 (1996) 3865.

37. M. Methfessel, M. van Schilfgaarde, R.A. Casali, The uses of the LMTO Method, in: H. Dreyssé (Eds.), Electronic Structure and Physical Properties of Solids, Springer Lecture Notes, Workshop Mont Saint Odille, France, 1998, Berlin, Springer, 2000, 114–147.

38. S. B. Zhang, S. H. Wei, A. Zunger, "Defect physics of the $CuInSe_2$ chalcopyrite semiconductor", Phys. Rev. B., 57 (1998) 9642.

39. M. Vahidi, Z. Z. Tang, J. Tucker, T. J. Peshek, L. Zhang, C. Kopas, R. K. Singh, M. van Schilfgaard, N. Newman, "Experimental study of the kinetically-limited decomposition of $ZnGeAs_2$ and its role in determining optimal conditions for thin film growth", J. Cryst. Growth, 338 (2012) 267.

40. Z. Z. Tang, S. J. Liu, R. K. Singh, S. Bandyopadhyay, I. Sus, T. Kotani, M. van Schilfgaarde, N. Newman, "Growth and characterization of epitaxial $Ba(Zn_{1/3}Ta_{2/3})O_3$ (100) thin films", Acta Mater., 57 (2009) 432.

41. Y. Shibata, K. Kaya, K. Akashi, M. Kanai, T. Kawai, S. Kawai, "Epitaxial growth and surface acoustic wave properties of lithium niobate films grown by pulsed laser deposition", J. Appl. Phys., 77 (1995) 1498.

42. F. W. Scholl and E .S. Cory, "Preparation and properties of $ZnGeAs_2$", Materials Research Bulletin, 9 (1974) 1511.

43. N. Newman, "The energetics of the GaN MBE reaction: a case study of meta-stable growth", J. Cryst. Growth, 178 (1997) 102.

44. N. Newman, J. Ross, M. Rubin, "Thermodynamic and kinetic processes involved in the growth of epitaxial GaN thin films", Appl. Phys. Lett., 62 (1993) 1242.

45. Z. Y. Fan, G. Rong, N. Newman, D. J. Smith, "Defect annihilation in AlN thin films by ultrahigh temperature processing", Appl. Phys. Lett., 76 (2000) 1839.

46. J. C. Angus and C. C. Hayman, "Low-Pressure, Metastable Growth of Diamond and "Diamondlike" Phases", Science, 241 (1988) 913.

47. J. Kim, R. K. Singh, J. M. Rowell, N. Newman, L. Gu, D. J. Smith, "Thermochemical analysis of MgB_2 synthesis by molecular-beam epitaxy", J. Cryst. Growth, 270 (2004) 107.

48. Z. Y. Fan and N. Newman, "Experimental determination of the rates of decomposition and cation desorption from AlN surfaces", Mater. Sci. Eng. B., 87 (2001) 244.

49. P. R. Willmott, "Deposition of complex multielemental thin films", Prog. Surf. Sci., 76 (2004)163.

50. M. Birkholz, D. Lichtenberger, C. HÖpfner, S. Fiechter, "Sputtering of thin pyrite films", Sol. Energ. Mat. Sol. C., 27 (1992) 243.

51. C. Wadia, A. P. Alivisatos, D. M. Kammen, "Materials Availability Expands the Opportunity for Large-Scale Photovoltaics Deployment", Environ. Sci. Technol., 43,

(2009) 2072.

52. B. Thomas, C. HÖpfner, K. Ellmer, S. Fiechter, H. Tributsch, "Growth of FeS_2 (pyrite) thin films on single crystalline substrates by low pressure metalorganic chemical vapour deposition", J. Cryst. Growth, 146 (1995) 630.

53. G. Willeke, R. Dasbach, B. Sailer, E. Bucher, "Thin pyrite (FeS_2) films prepared by magnetron sputtering", Thin Solid Films, 213 (1992) 271.

54. M. Bronold, S. Kubala, C. Pettenkofer, W. Jaegermann, "Thin pyrite (FeS_2) films by molecular beam deposition", Thin Solid Films, 304 (1997) 178.

55. C. de las Heras, J. L. Mart´ın de Vidales, I. J. Ferrer, C. S´anchez, "Structural and microstructural features of pyrite FeS_{2-x} thin films obtained by thermal sulfuration of iron", J. Mater. Res., Vol. 11, 1 (1996) 211.

56. L. Meng, Y. H. Liu, W. Huang, "Synthesis of pyrite thin films obtained by thermal-sulfurating iron films at different sulfur atmosphere pressure", Mat. Sci. Eng. B, 90 (2002) 84.

57. G. Smestad, A. Ennaoui, S. Fichter, H. Tributsch, W. K. Hofmann, M. Birkholz, "Photoactive thin film semiconducting iron pyrite prepared by sulfurization of iron oxides", Sol. Energy Mater., 20 (1990) 149.

58. P. Berberich, B. Utz, W. Prusseit, H. Kinder, "Homogeneous high-quality $YBa_2Cu_3O_7$ films on 3″ and 4″ substrates", Physica C, 219 (1994) 497.

59. B. H. Moeckly and W. S. Ruby, "Growth of high-quality large-area MgB_2 thin films by reactive evaporation", Supercond. Sci. Technol., 19 (2006) L21.

60. P. Waldner and A. D. Pelton, "Thermodynamic Modeling of the Fe-S System", J. Phase Equilib. Diff., Vol. 26, 1 (2005) 23.

61. A. Ennaoui, S. Fiechter, C. Pettenkofer, N. Alonso-Vante, K. Bilker, M. Bronold, Ch. H6pfner and H. Tributsch, "Iron disulfide for solar energy conversion", Sol. Energy Mater. Sol. Cells, 29 (1993) 289.

62. http://www.britannica.com/EBchecked/media/2405/Schematic-representation-of-the-structure-of-pyrite-FeS2-as-based

63. G. Smestad, A. Dasilva, H. Tributsch, S. Fichter, M. Kunst, N. Meziani, M. Birkholz, "Formation of Semiconducting Iron Pyrite by Spry Pyrolysis", Sol. Energy Mater., 18 (1989) 299.

64. B. Meester, L. Reijnen, A. Goossens, J. Schoonman, "Synthesis of Pyrite (FeS_2) Thin Films by Low-Pressure MOCVD", Chem. Vap. Deposition, 6 (2000) 121.

65. S. Seefeld, M. Limpinse, Y. Liu, N. Farhi, A. Weber, Y. Zhang, N. Berry, Y. J. Kwon, C. L. Perkins, J. C. Hemminger, R. Wu, M. Law, “Iron Pyrite Thin Films Synthesized from an Fe(acac)3 Ink”, J. Am. Chem. Soc., 135 (2013) 4412.

66. N. Berry, M. Cheng, C. L. Perkins, M. Limpinsel, J. C Hemminger, M. Law, “Atmospheric-Pressure Chemical Vapor Deposition of Iron Pyrite Thin Films”, Adv. Energy Mater., (2012) 1.

67. J. G. Massey and M. Lee, “Direct Observation of the Coulomb Correlation Gap in a Nonmetallic Semiconductor, Si:B”, Phys. Rev. Lett., 75, 23 (1995) 4266.

68. A. L. Efros and B. I. Shklovskii, “Coulomb gap and low temperature conductivity of disordered systems”, J. Phys. C: Solid State Phys., 8 (1975) L49.